# MASAP: A package for atomic scattering amplitude in solids

Akihiro Koide, Sara Rabouli, Pierre Le Meur, Sylvain Tricot, Philippe Schieffer, D. Sébilleau, Calogero R Natoli

# MASAP: A package for atomic scattering amplitude in solids

Akihiro Koide[a], Sara Rabouli[b], Pierre Le Meur[c], Sylvain Tricot[a], Schieffer Philippe[a], Didier Sébilleau[a], Calogero R. Natoli[d,*]

[a] *Univ Rennes, CNRS, IPR (Institut de Physique de Rennes)-UMR 6251, F-35000 Rennes, France*
[b] *INRAE UR REVERSAAL, 5 Rue de la Doua, CS 20244, 69625 Villeurbanne Cedex, France*
[c] *ABEJA, Inc., the ARGYLE aoyama WeWork 6F, 2-14-4 KitaAoyama, Minato-ku, Tokyo 107-0061, Japan*
[d] *INFN Laboratori Nazionali di Frascati, Via E Fermi 40, c.p. 13, I-00044 Frascati, Italy*

**Abstract**

We present the MsSpec Atomic Scattering Amplitude Package (MASAP), composed of a computation program and a graphical interface to generate atomic scattering amplitude (ASA) of an atom, either isolated or embedded in an environment, at any chosen energy of the impinging electron up to ≈15 KeV. The ASA is calculated using an effective, complex optical potential which provides damping effects in the scattering process in a fully relativistic framework. Optionally, scalar relativistic and non-relativistic approximations are also available to assess their applicability to a given problem. In order to describe electron propagation in solids we suggest to replace ASA's based on Plane Waves (PW) scattering with effective ASA's based on curved Spherical Waves (SW) using truncated-overlapped potentials of the Muffin-Tin (MT) type constructed according to the Mattheiss prescription. The graphical user interface generates not only ASA data files providing atomic Differential Cross Sections (DCS) but also files of related quantities such as total Cross Section (CS), both elastic and inelastic, atomic $t_l$-matrices and phase shifts. We found in general that the imaginary part of the optical potential enhances the calculated elastic DCSs in the forward direction compared to the same potential without the imaginary part, a feature related to the optical theorem, but gives rise to a lower intensity at all other directions as expected due to the damping effect of the complex part of the potential. We show calculated differential and transport Cross Sections for aluminum and gold atoms both in isolation and in crystals with the Face-Centered-Cubic (FCC) structure.

*Keywords:* atomic scattering amplitude; solid state effects; optical potential; relativistic effects; differential cross section

**PROGRAM SUMMARY/NEW VERSION PROGRAM SUMMARY**

*Program Title:* MASAP
*CPC Library link to program files:* (to be added by Technical Editor)
*Code Ocean capsule:* (to be added by Technical Editor)
*Licensing provisions:* Standard CPC licence, http://cpc.cs.qub.ac.uk/licence/licence.html
*Programming language:* FORTRAN 77, Python3
*External routines:*

- SciPy (https://www.scipy.org)

*Corresponding author.
*E-mail address:* natoli@lnf.infn.it

- Atomic Simulation Environment (https://wiki.fysik.dtu.dk/ase/)
- h5py (https://www.h5py.org)
- wxPython (https://www.wxpython.org)

*Nature of problem:*
Calculation of atomic scattering amplitudes of scattered electrons by an embedded atom in a solid including damping and relativistic effects. Comparison between ASA's in an isolated atomic system and a solid. Introduction of an effective ASA for electrons propagating in a solid derived from Multiple Scattering Theory.
*Solution method:*
Potential scattering theory. Muffin-tin approximation. Superposition of atomic electron density obtained by self-consistent Dirac-Fock atomic calculations. Hedin-Lundqvist potential as an optical potential. Fully relativistic theory, with scalar-relativistic and non-relativistic approximations for comparison.
*Additional comments including restrictions and unusual features:*
Even though the program can perform calculations at impinging electron energies up to ≈15 Kev, DCS calculations are recommended in the range 50 : ≈1500 eV both in the case of isolated atoms and atoms embedded in solids, since this interval is more suitable for studying the details of the atomic potentials in their environment.
In the case of solids, at energies lower than ≈50 eV, the details of the electronic structure might be important, whereas in the case of isolated atoms this range might suffer from the neglect of the polarization potential and coupling to available inelastic channels. In this respect an option to add an empirical form of a polarization potential to investigate its effects is available to the interested user.

## 1. Introduction

The scattering of electrons by atoms, molecules and solids is of widespread importance in many areas of physics, ranging from radiation physics and material analysis to Auger-electron spectroscopy (AES), and X-ray Photoelectron Spectroscopy (XPS). We refer to [1, 2] and references therein for a more complete discussion of the various areas of application. In particular elastic-scattering cross sections have been frequently used in theoretical descriptions (e.g., by Monte Carlo simulations) of electron transport in solids. These and related calculations have been performed for applications in surface analysis by AES and XPS and Analytical Electron Mycroscopy (AEM).

In the paper by Jablonski *et al* [1] the emphasis was on the type of potential used to calculate the Atomic Scattering Amplitudes (ASA), whether of the Thomas-Fermi-Dirac (TFD) or of the Dirac-Hartree-Fock (DHF) type. Ref. [2] makes instead use of a more elaborate optical-model potential developed by one of the authors (F. Salvat) in Ref. [3].

In connection with this problem, the main motivation behind this paper is the introduction of an exchange-correlation potential of the Hedin-Lundqvist type (HL) [4, 5] for the calculation of ASA's that has been used up to now with remarkable success in the interpretation of x-ray absorption spectra and photoelectron diffraction [6, 7, 8]. The hope is that the study of atomic DCS's will bring new information compared to EXAFS structural analysis.

The second motivation takes inspiration from Multiple Scattering Theory and realizes that in order to describe the propagation of an electron in solids one does not need an ASA based on PW's, but on SW's, leading to an effective ASA. Moreover the atomic potential to be used is a truncated-overlapped potential of the Muffin-Tin (MT) type constructed according to the Mattheiss prescription [9].

The present program tries to fulfill both aims by using the HL potential to calculate ASA of isolated atoms, but also provides the possibility to input a cluster of atoms, using the overlapped

atomic densities to construct the cluster MT potential. In this way one can calculate both PW and SW ASA's to be used in the simulation of electron transport in solids and electron-molecule scattering. We refer to Ref. [10] regarding the construction of MT cluster potentials and densities. Throughout the paper we use atomic units for lengths and Rydberg units for energies.

## 2. Theoretical background

### *2.1. Relativistic Electron-Atom potential scattering*

The Dirac Equation (DE) is the starting point for a fully relativistic calculation of the Atomic Scattering Amplitudes. In our units, indicating by $\alpha = e^2/(\hbar c) = 1/137.036$ the fine structure constant, the DE for an electron with total energy (including rest mass) E in presence of a central potential $V(r)$, to be specified later, writes

$$\frac{\alpha^2}{2}\Big(E - V(r)\Big)\Psi = \Big(\frac{\alpha}{i}\,\vec{\boldsymbol{\alpha}}\cdot\vec{\nabla} + \boldsymbol{\beta}\Big)\Psi \tag{1}$$

Here $\Psi$ is the Dirac bi-spinor

$$\Psi = \begin{pmatrix} g_\kappa(r)\,\chi^\mu_\kappa \\ i\,f_\kappa(r)\,\chi^\mu_{-\kappa}\end{pmatrix} \tag{2}$$

where $g_\kappa(r)$ and $f_\kappa(r)$ are the upper and lower radial function components, and

$$\vec{\boldsymbol{\alpha}} = \begin{pmatrix} 0 & \vec{\sigma} \\ \vec{\sigma} & 0\end{pmatrix} \qquad \vec{\boldsymbol{\beta}} = \begin{pmatrix} 1 & 0 \\ 0 & -1\end{pmatrix} \tag{3}$$

are the velocity and mass term operators, $\vec{\sigma}$ denoting the Pauli matrices. In the bi-spinor Eq. (2), $\chi^\mu_\kappa$ is the spin-orbital

$$\chi^\mu_\kappa = Y^{J\mu}_{l\,1/2} = \sum_\nu \langle l\,\mu - \nu | J\,\mu\rangle\; Y_{l\,\mu-\nu}(\hat{\mathbf{r}})\,\chi_\nu \tag{4}$$

labeled only by the orbital projection $\mu$ and the relativistic quantum number $\kappa$. In this equation $Y_{l\mu}(\hat{\mathbf{r}})$ is the Spherical Harmonics with angular momentum $l$ and projection $\mu$, $\chi_\nu$ is the usual spin function and $\langle l\,\mu - \nu | J\,\mu\rangle$ is a Clebsh-Gordan coefficient. Since the spin-orbital is an eigen-state of $\mathbf{J}^2$, $\mathbf{L}^2$ and $\mathbf{S}^2$ one can easily derive that

$$(1 + 2\vec{s}\cdot\vec{l})Y^{J\mu}_{l\,1/2} = -\kappa\, Y^{J\mu}_{l\,1/2} \tag{5}$$

Therefore the relativistic quantum number $\kappa$ determines both $J = |\kappa| - 1/2$ and $l$ according to $\kappa = l$ for $J = l - 1/2$ and $\kappa = -(l+1)$ for $J = l + 1/2$. We refer the interested reader to [11] for the steps leading from the bi-spinor DE to the following radial equations

$$\begin{aligned} u_\kappa(r) &= \frac{-2}{\alpha\,(\epsilon - V(r))}\left(\frac{d}{dr} - \frac{\kappa}{r}\right) v_\kappa(r) \\ v_\kappa(r) &= \frac{\alpha}{2}\,\frac{1}{1 + \frac{1}{4}\,\alpha^2\,(\epsilon - V(r))}\left(\frac{d}{dr} + \frac{\kappa}{r}\right) u_\kappa(r) \end{aligned} \tag{6}$$

in terms of

$$u_\kappa(r) = r\,g_\kappa(r); \qquad v_\kappa(r) = r\,f_\kappa(r) \tag{7}$$

where now $\epsilon = E - 2/\alpha^2$ is the electron energy less its rest mass. This is positive for continuum scattering states.

Following [12], we use the second equation of (6) to replace $v_\kappa(r)$ into the first equation. Introducing the quantity

$$B(r) = \frac{1}{1 + \frac{1}{4}\,\alpha^2\,(\epsilon - V(r))} \tag{8}$$

we find, in terms of the non-relativistic operator,

$$H_{nr}(r) = \frac{d^2}{dr^2} + \epsilon - V(r) - \frac{\kappa(\kappa+1)}{r^2} \tag{9}$$

the expression

$$\begin{aligned} \left(H_{nr}(r) + \frac{\alpha^2}{4}\,(\epsilon - V(r))^2 \quad - \right. \\ \left. \frac{\alpha^2}{4}\,B(r)\left[\frac{d}{dr}V(r)(\frac{d}{dr} - \frac{1}{r}) + \frac{1+\kappa}{r}\,\frac{d}{dr}V(r)\right]\right) u_\kappa(r) &= 0 \\ (H_{nr}(r) + H_m(r) + H_D(r) + H_{so}(r))\,u_\kappa(r) &= 0 \end{aligned} \tag{10}$$

which is a kind of pseudo-Schrödinger Equation. The $H_m(r)$ term is known as the mass relativistic correction, the $H_D(r)$ one as the Darwin correction and $H_{so}(r)$ is the spin-orbit potential. Indeed, according to Eq. (5), $(1+\kappa)$ acting on a spin-orbital state is equivalent to $-2\vec{s}\cdot\vec{l}$. Notice that $\kappa(\kappa+1) = l(l+1)$ for all $\kappa$.

The associated indicial equation is obtained by inserting the assumed low $r$ behavior of $u_\kappa(r) \sim r^\rho\,[a_0 + a_1\,r + ...]$ into Eq. (10) and equating to zero the coefficient of the lowest power of r ($r^{\rho-2}$). Taking into account that $\lim_{r\to 0}\, rV(r) = -2Z$, where $Z$ is the atomic number of the atom under consideration, so that $\lim_{r\to 0}\, B(r) \sim 2r/(Z\alpha^2)$, one finds

$$\rho(\rho-1) + \rho - (\kappa^2 - (Z\,\alpha)^2) = 0 \tag{11}$$

which gives $\rho = [\kappa^2 - (Z\,\alpha)^2]^{1/2}$ (taking only the positive root for regular behavior at the origin). This is obviously the same low $r$ behavior of the DE.

The solution of Eq. (10) provides the upper component of the radial DE. The lower one can be obtained by inserting this solution into the second equation in (6). We do not use the lower component, because the upper component is sufficient to provide the exact relativistic atomic $t$-matrix, as shown below.

The equation (10) is numerically solved by the Numerov procedure after elimination of the first order derivative (as detailed in [12]), by applying the method of Gaussian elimination without pivoting with the initial behavior given by Eq. (11) [13]. We also use the more flexible linear-log mesh $\tilde{\rho} = \alpha r + \beta \log(r)$ instead of the usual Herman-Skillman (HS) mesh, since the relativistic corrections take effect at much smaller values of $r$ than the initial point of the HS mesh. We should therefore perform a change of variable from $r$ to $\tilde{\rho}$ before applying the Numerov procedure, which requires constant spacing of the integration variable. For details the reader is referred to [14].

In order to find the atomic $t$-matrices in the relativistic framework we need the free radial solutions of the DE for positive energies, both regular and irregular. They are obtained from Eq. (1) (via Eq. (10)) by setting $V(r)$ to zero and are given in [11].

As in the non-relativistic framework, the relativistic $t$-matrix is obtained by matching smoothly the solution of the DE inside the atomic sphere with the free solution outside the sphere at a radius $R_s$, which is the chosen MT radius for an atom embedded in an environment or determined such that $|V(R_s)|/\epsilon \approx 10^{-5}$, in the case of an isolated neutral atom. The matching condition, including the derivative, is

$$\left.\begin{pmatrix} g_\kappa(r)\,\chi^\mu_\kappa \\ i\,f_\kappa(r)\,\chi^\mu_{-\kappa}\end{pmatrix}\right|_{r=R_s} = \begin{pmatrix} j_{l_\kappa}(kr)\,\chi^\mu_\kappa \\ i\,CS_\kappa\, j_{\bar{l}}(kr)\,\chi^\mu_{-\kappa}\end{pmatrix} - ik\,t_\kappa \left.\begin{pmatrix} h^+_{l_\kappa}(kr)\,\chi^\mu_\kappa \\ i\,CS_\kappa\, h^+_{\bar{l}}(kr)\,\chi^\mu_{-\kappa}\end{pmatrix}\right|_{r=R_s} \tag{12}$$

where $C = \alpha/[2\,(1+\frac{1}{4}\,\alpha^2\,\epsilon)]$, $S_\kappa = \kappa/|\kappa|$, $k^2 = \epsilon(1+\frac{\alpha^2}{4}\,\epsilon)$ is the free electron energy and $k$ is its momentum. Therefore, indicating by $l_\kappa$ the $l$-value associated to $\kappa$ so that $\bar{l} = l_\kappa - S_\kappa$, we find

$$\begin{aligned} t_\kappa &= \frac{i}{k}\,\left.\frac{[g_\kappa(r)\,j'_{l_\kappa}(kr) - g'_\kappa(r)\,j_{l_\kappa}(kr)]}{[g_\kappa(r)\,(h^+_{l_\kappa})'(kr) - g'_\kappa(r)\,h^+_{l_\kappa}(kr)]}\right|_{r=R_s} \\ &= \frac{i}{k}\,\left.\frac{[f_\kappa(r)\,j'_{\bar{l}}(kr) - f'_\kappa(r)\,j_{\bar{l}}(kr)]}{[f_\kappa(r)\,(h^+_{\bar{l}})'(kr) - f'_\kappa(r)\,h^+_{\bar{l}}(kr)]}\right|_{r=R_s} \end{aligned} \tag{13}$$

As a consequence, $t_\kappa$ is determined solely by the knowledge of the upper component $g_\kappa(r)$. As a check, we have verified that the second expression in terms of the lower component $f_\kappa(r)$ provides the same $t$-matrix.

The advantage of using the pseudo-SE for solving the DE is that it is possible to assess the relevance of the various potential terms in Eq. (10) to the case under consideration. To this purpose the present package generates three kinds of $t^{pa}_\kappa$-matrices, according to the kind of potential approximations ($pa$) retained. Correspondingly, three DCS are provided. A fourth DCS is generated for a Slater X-alpha constant exchange potential, which is used only for comparison reasons to illustrate the drawbacks of this kind of exchange in a scattering process.

Retaining in the last equation (10) only the first term one recovers the usual non-relativistic SE ($pa = nr$). According to Eq. (13) the corresponding radial solution generates the non-relativistic $t^{nr}_\kappa$-matrices. Notice that in this case the electron momentum is $k = \sqrt{\epsilon}$.

By adding the second $H_m(r)$ and the third $H_D(r)$ term we obtain the scalar relativistic equation ($pa = sr$) that provides the $t^{sr}_\kappa$-matrices in the same approximation.

Finally when the potential includes also the spin-orbit term $H_{so}(r)$ we recover the fully relativistic potential, including spin-orbit effects ($pa = so$). In this case, the value of the quantum number $\kappa$ determines both $J$ and $l$. Correspondingly, according to the value of the quantum number $J = |\kappa| - 1/2$, the program generates two sets of $t$-matrices, $t^{so-}$ for $J = l - 1/2$ ($\kappa$ positive) and $t^{so+}$ for $J = l + 1/2$ ($\kappa$ negative).

If the potential has a coulombian tail, *e.g.* when treating scattering off positive ions, it is sufficient to replace in the first of Eq. (13) the Bessel and Hankel functions with the corresponding radial functions upper solutions of the Dirac equations written for a pure Coulomb potential with the appropriate asymptotic charge. Then the calculation of the DCS's proceeds as illustrated below, with the *caveat* to avoid the forward divergence characteristic of the Coulomb potential. Since our emphasis in this paper is on the use of the HL potential and not on the scattering by positive ions, we refer the reader to the exhaustive discussion contained in Ref. [2].

In relativistic theory, the elastic-scattering DCS $\left(\frac{d\sigma}{d\Omega}\right)_k$ for unpolarized incident beam incident

on an isolated atom is given as [15]

$$\left(\frac{d\sigma}{d\Omega}\right)_k = |f_k(\theta)|^2 + |g_k(\theta)|^2 \tag{14}$$

where $f_k(\theta)$ and $g_k(\theta)$ are the direct and spin-flip scattering amplitudes. These amplitudes are expressed in terms of the $t^{so\pm}$-matrices for spin-up (+) and spin-down (-) scattering as

$$\begin{aligned} f_k(\theta) &= \sum_l \left[(l+1)\, t_l^{so+}(k) + l\, t_l^{so-}(k)\right] P_l(\cos\theta) \\ g_k(\theta) &= \sum_l \left[t_l^{so-}(k) - t_l^{so+}(k)\right] P_l^1(\cos\theta) \end{aligned} \tag{15}$$

In these equations, $P_l(x)$ is the Legendre polynomial of order $l$, and $P_l^1(x)$ is the associated Legendre polynomial given by $P_l^1(x) = \sqrt{(1-x^2)}\, dP_l(x)/dx$.

Neglecting spin-orbit effects, $t_l^{so+}(k) = t_l^{so-}(k) = t_l^{(nr,sr)}(k)$, according to the chosen approximation for the potential (either *nr* or *sr*) and the scattering amplitude reduces to

$$f_k(\theta) = \sum_l \left[(2l+1)\, t_l^{(nr,sr)}(k)\right] P_l(\cos\theta) \tag{16}$$

while $g_k(\theta)$ is identically zero. Equations (14), (15) for central field potentials were first derived by Mott [16] and the resulting DCS is sometimes referred to as the Mott cross section.

Since the two spin-orbit channels are decoupled for spherical radial potentails, in general the relation between the $t$-matrix and the $s$-matrix is given by

$$t_\kappa(k) = \frac{s_\kappa(k) - 1}{2ik} \tag{17}$$

$$s_\kappa(k) = e^{2i\delta_\kappa(k)} \tag{18}$$

where $\delta_\kappa(k)$ is the potential phase shift for channel $\kappa$. It is known in scattering theory that the difference in amplitude between the incoming $l$-wave and the outgoing scattered wave is the factor $s_\kappa$. Therefore $|s_\kappa| = 1$ if the scattering potential is real (the flux of particles is conserved), whereas $|s_\kappa| < 1$ if the potential has a complex part, representing the absorption of part of the incoming flux. The elastic CS $\sigma_k^{ela}$ is given by

$$\sigma_k^{ela} = \int d\Omega \left(\frac{d\sigma}{d\Omega}\right)_k = 2\pi \int_0^\pi \sin\theta\, d\theta \left(|f_k(\theta)|^2 + |g_k(\theta)|^2\right) \tag{19}$$

In accordance with the optical theorem, the total CS $\sigma_k^{tot}$ is related by the imaginary part of the forward scattering amplitude $f_k(0)$ by

$$\sigma_k^{tot} = \frac{4\pi}{k} \Im f_k(0) \tag{20}$$

since $g_k(\theta)$ is zero at $\theta = 0$, being proportional to $P_l^1(\cos\theta)$.

Because $\sigma_k^{tot} = \sigma_k^{ela} + \sigma_k^{ine}$ where $\sigma_k^{ine}$ is the inelastic CS, $\sigma_k^{ine}$ is obtained by

$$\sigma_k^{ine} = \frac{4\pi}{k} \Im f_k(0) - 2\pi \int_0^\pi \sin\theta d\theta \left(|f_k(\theta)|^2 + |g_k(\theta)|^2\right) \tag{21}$$

Another cross section of interest is the transport CS (or momentum-transfer CS) $\sigma_k^{tr}$ defined as [1]

$$\begin{aligned}\sigma_k^{tr} &= \int d\Omega\,(1-\cos\theta)\left(\frac{d\sigma}{d\Omega}\right)_k \\ &= 2\pi\int \sin\theta\, d\theta\,(1-\cos\theta)\left(|f_k(\theta)|^2+|g_k(\theta)|^2\right)\end{aligned} \tag{22}$$

$\sigma_k^{tr}$ is related to the momentum transfer $\Delta k$ as follows.

$$\langle \Delta k\rangle = k\frac{\sigma_k^{tr}}{\sigma_k^{ele}} \tag{23}$$

Finally, $\delta_\kappa(k)$ can be obtained from Eq. (18).

$$\begin{aligned}\delta_\kappa(k) &= \frac{1}{2i}\ln s_\kappa(k) \\ &= n\pi+\frac{1}{2}\arg(s_\kappa(k))-\frac{i}{2}\ln|s_\kappa(k)|\end{aligned} \tag{24}$$

where $n\pi$ is determined by the Levinson's theorem, stating that $n$ is the number of bound states with $l$ symmetry. When $|s_\kappa(k)|<1$, $\delta_\kappa(k)$ has a non-zero imaginary part.

All of the above relations, valid in the framework of a complete relativistic description, remain so even if the radial part of the potential is approximated in the way described above.

### *2.2. The interaction potential V(r)*

The interaction potential $V(r)$ is defined as

$$V(r) = V_c(r) + V_{exc}(r,\epsilon) \tag{25}$$

where $V_c(r)$ is the electrostatic Coulomb potential, which for a single atom with atomic number $Z$ is given by

$$V_c(r) = -\frac{2Z}{r}+\frac{2}{r}\int_0^r \rho(r')\,r'^2dr' + 2\int_r^\infty \rho(r')\,r'\,dr' \tag{26}$$

and $\rho(r)$ is the atomic charge density normalized such that $\int_0^\infty \rho(r)\,r^2dr = Z$ and calculated using the self-consistent single configuration Dirac-Fock atom code [17].

In Eq. (25) $V_{exc}(r,\epsilon)$ is a local exchange-correlation (EXC) (possibly energy dependent) potential.

One such instance is the energy-dependent EXC potential of Furness and McCarthy used in [1, 2] and given by

$$V_{exc}(r) = [\epsilon - V_c(r)] - \left\{[\epsilon - V_c(r)]^2+\rho(r)\right\}^{1/2} \tag{27}$$

The corresponding potential, obtained by summing Eq.s (26) and (27), is called the Dirac-Hartree-Fock (DHF) potential in Ref. [1] and static-exchange (SE) potential in Ref. [3]. This latter work adds to this a correlation-polarization potential obtained by combining the correlation potential derived from the local density approximation with a long-range polarization interaction, so that the new potential is denominated SECP. Moreover, in order to mimic the opening of inelastic channels in the scattering process, a further absorptive (complex) part is added with a strength adjusted by means of an empirical parameter.

In this paper we propose instead to use the Hedin-Lundqvist (HL) EXC complex potential [10] for the calculations of the Atomic Scattering Amplitudes. This potential is derived within the GW approximation in many-body theory and is parameter free. In order to calculate the self-energy, the local density approximation replaces the exact self-energy by that of the homogeneous electron gas calculated at the local density of the system under investigation. Therefore we can define a sort of universal EXC potential as

$$V_{exc}(r,\varepsilon) \approx \Sigma_h\left[p(r), \varepsilon - V_c(r); \rho(r)\right] \tag{28}$$

$\Sigma[p,\omega;\rho]$ is the self-energy of an electron in an homogeneous interacting electron gas with local momentum $p(r)$, energy $\omega = \varepsilon - V_c(r)$, and the density $\rho$ of the actual physical system. The local momentum $p(r)$ is defined approximately as $p^2(r) = k^2 + k_F^2(r)$, where $k^2$ is the electron kinetic energy measured from the Fermi level for an extended system or from the first ionization potential for finite systems (atoms and molecules) and $k_F^2(r)$ is the local Fermi energy, defined below as a function of the local density $\rho$. The GW approximation [4, 5] with the non-perturbed Green function $G_0$ and the screening Coulomb $W$ gives the electron self energy as

$$\begin{aligned}
\Sigma_h(p,\omega) &= \frac{i}{(2\pi)^4}\int dp'd\omega'\, e^{i\omega'\delta} \\
&\quad \times G_0(p+p',\omega+\omega')W(p',\omega') \qquad (29)\\
G_0(p,\omega) &= \frac{1}{\omega - p^2 + i\mathrm{sign}(\omega-\varepsilon_F)} \qquad (30)\\
W(p',\omega') &= \frac{V(p')}{\epsilon(p',\omega')} \qquad (31)
\end{aligned}$$

The Fermi energy $\varepsilon_F$ is defined by

$$\begin{aligned}
\varepsilon_F &= k_F^2, \qquad (32)\\
k_F &= \left(3\pi^2\rho\right)^{1/3} = \frac{1}{\beta r_s}, \qquad (33)\\
\beta &= \left(\frac{4}{9\pi}\right)^{1/3}, \qquad (34)\\
r_s &= \left(\frac{3}{4\pi\rho}\right)^{1/3}. \qquad (35)
\end{aligned}$$

In the plasmon-pole approximation [4, 5], the dielectric function $\epsilon$ of the electron gas is written as

$$\begin{aligned}
\frac{1}{\epsilon(p,\omega)} &= 1 + \frac{\omega_p^2}{\omega^2 - \omega_1^2(p)}, \qquad (36)\\
\omega_p &= 4\varepsilon_F\sqrt{\frac{\beta r_s}{3\pi}} \qquad (37)\\
\omega_1(p) &= \omega_p^2 + \varepsilon_F\left(\frac{4p^2}{3k_F^2} + \frac{p^4}{k_F^4}\right), \qquad (38)
\end{aligned}$$

where $\omega_1$ is the dispersion of the plasmon pole.

Explicit calculations, carried out in Appendix B of Ref. [18], show that the real part of $V_{exc}(r, \varepsilon)$ is the sum of three contributions:

$$\Re V_{exc}(r, \varepsilon) = V_{ex}^{DH} + V_{sex} + V_{ch} \tag{39}$$

where $V_{ex}^{DH}$ is the usual static and energy-dependent Dirac-Hara exchange, obtained by Dirac and discussed by Hara, $V_{sex}$ is a sort of screened exchange and $V_{ch}$ describes the effect of the Coulomb correlation hole, originating from the fact that the test electron tends to keep away the electrons of the system of both spins because of the Coulomb repulsion.

In terms of the reduced variable $X_k = p(r)/k_F(r)$, the high kinetic energy behavior of the various terms in Eq. (39) is as follows [18]:

$$V_{ex}^{DH} \asymp -k_F/X_k^2 \sim -\rho(r)/p^2(r); \quad V_{sex} \asymp -1/X_k^4; \quad V_{ch} \asymp -1/X_k \tag{40}$$

Notice that the EXC potential of Furness and McCarthy in Eq. (27) has the same asymptotic behavior as the Dirac-Hara exchange $V_{ex}^{DH}$ if one assumes that in the spirit of the local density approximation $E - V(r) \sim p^2(r)$. This energy dependence of the exchange is required by the fact that the higher the energy of the test electron the lesser is the effect of the Pauli exclusion principle, since the wave function overlap of the test electron with the electrons of the system decreases with the energy of the former. However this decrease is too rapid and it is mitigated by the presence of the Coulomb correlation hole. The combined energy dependence has been recognized as essential for a reliable calculation of the potential phase shifts in the structural analysis of the extended x-ray absorption fine structure (EXAFS) in many systems.

The imaginary part of $V_{exc}(r, \varepsilon)$ is non zero only if $k^2 > \omega_p$, where $\omega_p$ is the local plasmon energy in the system. In other words, there is no damping if the test electron kinetic energy is not sufficient to excite the local plasmon mode of the medium. Lower energy excitations, like particle-hole excitations, are not possible because of the assumption of the plasmon-pole approximation for the dielectric function $\epsilon(p, \omega)$. Although negligible in a first approximation, they should be added for a complete treatment of the damping. The performance of the HL potential in the EXAFS analysis has been discussed by Mustre de Leon *et al* [19].

The quantity $\Im V_{exc}(r, \varepsilon)$ is related to the mean free path (MFP) of the test electron by

$$\lambda(r) = \frac{k}{\Im V_{exc}(r, \varepsilon)} \tag{41}$$

written in a.u. (see Eq. (78) of Ref. [20]). It is a function of $r$ through the dependence of $V_{exc}$ on the local density $\rho(r)$. The quantity to compare with experimental MFP data is the average of $\lambda(r)$ over the system under study [21].

The original derivation of the HL potential was proposed by Hedin and Lundqvist [4, 5] for valence electrons. After, Lee and Beni extended its validity to the atomic region [22]. For details on the analytical formulas we refer to Appendix B of [18]. They are coded into the subroutine *hlvxc* of the program. For fixed electron energy, the real and imaginary parts are output in the file *vxc_xm.dat* together with the Furness and McCarthy exchange potential of Eq. (27) for an easy comparison. Numerically interpolated values have also been given by [19].

It is worth remembering that a many-pole model of the dielectric function (and therefore of the self-energy) has been introduced by J. J. Rehr and collaborators to improve on the single pole approximation. We refer the interested reader to their main papers on the subject [23, 24].

The complex part of the potential describes the attenuation of the elastic scattering amplitude of the impinging electron due to inelastic losses, but enhances the elastic DCS in the forward

direction compared to the case of the real potential. There is an option in the program to set it to zero, so that one can estimate the global effect of the inelastic processes on the elastic scattering cross section. We refer to Ref. [10] for plots of the real and imaginary parts of $V_{exc}(r, \varepsilon)$ as a function of $\varepsilon$ for two different values of $r_s = 0.1, 0.01$.

Finally there is the possibility for the interested user to add to the Coulomb part an empirical polarization potential of the type

$$V_{pol}(r) = -\frac{\alpha_0}{2} \frac{1}{[r^2 + d^2]^2} \tag{42}$$

where $\alpha_0$ is the atomic polarizability and $d$ is a constant of the order of atomic radius [25]. Note that at large $r$, $V_{pol}(r) \asymp r^{-4}$. It is however ignored in truncated potentials for atoms in a medium. If $\alpha_0$ is different from zero, this potential is added to the Coulomb potential using the input $d$. This option is useful if one wants to assess the effect of the polarization potential at electron energies lower than 50 eV, even though its effects might be noticeable even at higher energies [3]. We refer to this latter work and references therein for a more complete discussion on this point and the value of the parameters $\alpha_0, d$. Except when explicitly stated, all the calculations presented in this work omit this kind of potential.

### *2.3. The electron transport in solids*

One of the applications of ASA is the description (*eg* by Monte Carlo simulations) of electron transport in solids. We would like to suggest a different method inspired by Multiple scattering Theory (MST) which should be more adherent to physical reality. In MST, within a non-relativistic or scalar relativistic approximation, the cross section for electrons scattering off a finite cluster of atoms, however big, located at sites $R_i$ can be written, following Ref. [20] (Section 4.6 page 209), as

$$\frac{d\sigma}{d\hat{\mathbf{k}}_s} = (4\pi)^2 \left| \sum_{i,L} \sum_{j,L'} i^{-l'} Y_{L'}(\hat{\mathbf{k}}_s)\, \mathrm{e}^{-\mathrm{i}\hat{\mathbf{k}}_s \cdot \mathbf{R}_j} \boldsymbol{\tau}^{ji}_{L'L}\, i^{l} Y_L(\hat{\mathbf{k}}_i) \mathrm{e}^{\mathrm{i}\hat{\mathbf{k}}_i \cdot \mathbf{R}_i} \right|^2 \tag{43}$$

where $\hat{\mathbf{k}}_i$ and $\hat{\mathbf{k}}_s$ are the incident and scattered wave vectors. The quantity $\boldsymbol{\tau}^{ji}_{L'L}$ is the scattering path operator, central in MST, that describes the electron amplitude of propagation of a spherical wave with angular momentum $L$ around site $i$ to a site $j$ with angular momentum $L'$ (and vice-versa, since the matrix is symmetric in both indices), after any number of scattering processes by the atoms of the cluster. As customary in MST, $L$ stands for $l, m$.

To get some insight into the physical interpretation of Eq. (43), we observe that in the case of a single atom located at site $i$ coincident with the center of coordinates, we have (as argued below) $\boldsymbol{\tau}^{i\,j}_{LL'} = t^i_l\, \delta_{ij}\, \delta_{LL'}$, where $t_l$ is the scattering amplitude of the atom introduced above in Section 2. By performing the sum over the angular momentum $L$ and using the addition theorem for Spherical Harmonics we obtain Eq. (16).

In the presence of several atoms located at sites $i$ Eq. (43) tells that the total scattering amplitude of the cluster of atom for a plane wave impinging along the direction $\hat{\mathbf{k}}_i$ and scattered along $\hat{\mathbf{k}}_s$ is obtained by summing all the single scattering amplitudes of their spherical components $L, L'$ obtained by multiplying the amplitude of propagation between the two sites $\boldsymbol{\tau}^{i\,j}_{LL'}$ by the phase factors $\mathrm{e}^{\mathrm{i}\hat{\mathbf{k}}_i \cdot \mathbf{R}_{i(j)}}$ representing the phase of the PW with respect to the two sites.

In terms of the site scattering matrix $T^i_{LL'}\delta_{ij} = t^i_l\,\delta_{ij}\,\delta_{LL'}$ (assuming MT potentials) and the free spherical wave propagator (SWP) $G^{ij}_{LL'}$ from site $i$ to site $j$, it is clear that $\boldsymbol{\tau}^{ij}_{LL'}$ obeys the following equation

$$\boldsymbol{\tau}^{ij}_{LL'} = T^i_{LL'}\delta_{ij} + \sum_{\underline{L}\underline{L}'k} T^i_{L\underline{L}}\,G^{ik}_{\underline{L}\underline{L}'}\,\boldsymbol{\tau}^{kj}_{\underline{L}'L'} \tag{44}$$

which is derived from a re-summation of the Born series in which the electron first scatters from atom at site $i$, then propagates to cell $k$ undergoing here another scattering event, then to the next cell, and so on and so forth. The solution of this equation is given in terms of the inverse of the MS matrix ($\mathbf{T}^{-1} - \mathbf{G}$) as

$$\boldsymbol{\tau} = (\mathbf{T}^{-1} - \mathbf{G})^{-1} = \sum_n (\mathbf{TG})^n\,\mathbf{T} = \sum_n \mathbf{T}\,(\mathbf{GT})^n \tag{45}$$

where the series expansion reproduces the original Born series (matrix multiplication in the appropriate indexes is implied) and converges if $\rho(\mathbf{TG})$, the spectral radius (maximum eigenvalue) of $\mathbf{TG}$, is less than one. For more details of the theory we refer to [10, 20].

A fairly good approximation to the SWP [26] is given by:

$$G^{ij}_{LL'} \approx -4\pi\,\frac{\mathrm{e}^{\mathrm{i}kR_{ij}}}{kR_{ij}}\,g^0_{ll'}(kR_{ij})\,Y_L(\hat{\mathbf{R}}_{ij})\,Y_{L'}(\hat{\mathbf{R}}_{ij})\,i^{(l-l')} \tag{46}$$

The function $g^0_{ll'}(\rho)$ represents a kind of curved wave correction [26] given by

$$g^0_{ll'}(\rho) = \left[1 + \frac{L^2 + (L')^2}{2\rho^2}\right]^{1/2} \mathrm{e}^{\mathrm{i}[L^2+(L')^2]/(2\rho)}\,J_0\left(\frac{L^2L'^2}{\rho^2}\right) \tag{47}$$

where $J_0$ is the spherical Bessel function of order zero and $L^2 = l(l+1)$. In the following we shall neglect the less important amplitude factors and retain only the phase factor.

A convenient simplification of the theory is achieved when $\rho(\mathbf{TG}) \ll 1$ (this is the case for energies greater than ~100 eV). In this case we can retain only the first and second term of the Born series so that

$$\boldsymbol{\tau}^{ij}_{LL'} = t_l\delta^i_{LL'}\delta_{ij} + \sum_j t^i_l\,G^{ij}_{LL'}\,t^j_{l'} \tag{48}$$

By inserting this expression into Eq. (43) one derives after some algebra

$$\begin{aligned}\frac{d\sigma}{d\hat{\mathbf{k}}_s} &= \left|\sum_i \mathrm{e}^{\mathrm{i}(\hat{\mathbf{k}}_i-\hat{\mathbf{k}}_s)\cdot\mathbf{R}_i}\,f^i(\hat{\mathbf{k}}_s\cdot\hat{\mathbf{k}}_i)\right. \\ &+ \left.\sum_{ij} \mathrm{e}^{\mathrm{i}(\hat{\mathbf{k}}_i\cdot\mathbf{R}_i-\hat{\mathbf{k}}_s\cdot\mathbf{R}_j)}\,f^j_{eff}(\hat{\mathbf{k}}_s\cdot\mathbf{R}_{ji})\,f^i_{eff}(\hat{\mathbf{k}}_i\cdot\mathbf{R}_{ji})\frac{\mathrm{e}^{\mathrm{i}kR_{ij}}}{kR_{ij}}\right|^2\end{aligned} \tag{49}$$

where $\mathbf{R}_{ji} = \mathbf{R}_j - \mathbf{R}_i$, $f^i(\theta)$ is the same as in Eq. (16) with $t_l$ calculated for the truncated MT *sr*-type potential at site $i$ and we have defined an effective site-dependent scattering amplitude as

$$f^i_{eff}(\theta; R_{ij}) = \sum_l (2l+1)\,t^i_l(k)\,P_l(\theta)\,\mathrm{e}^{\mathrm{i}[l(l+1)]/(2kR_{ij})} \tag{50}$$

In this way we have neglected atomic spin-orbit effects which however can be easily incorporated in the formalism.

As anticipated, the plane-wave electron scattering amplitude is modified by the presence of the spherical wave propagator and assumes a distance dependence between scattering sites. The main effect of the additional phase factor is to reduce the scattering amplitude in the forward direction with an aperture cone and a reducing factor depending on the energy, the more so the higher the impinging energy.

Equation (49) suggests that the present Monte Carlo programs for simulating electron transfer in solids might benefit from the use of ASA for embedded atoms, the replacement of the plane-wave ASA by the curved-wave effective ASA of Eq. (50) and the addition of a spherical wave propagator $e^{ikR_{ij}}/(kR_{ij})$ between any two sites $i$ and $j$, while preserving their stochastic framework.

To see how this replacement can be achieved we give a short description of the Monte Carlo algorithm as presently implemented, referring the reader to Ref.s [27, 28] and references therein for more details and applications.

Briefly, in a Monte Carlo simulation the electron trajectory is considered a "random walk" in which the electron direction is changed by elastic collisions only. The simulation is based on two main assumptions:

- (1) multiple elastic electron collisions along the trajectory are well described by the Poisson stochastic process;
- (2) the scattering centers are randomly distributed in the solid, and can be approximated by the potentials of isolated atoms.

Under these assumptions, the distances between elastic collisions $\Lambda$ are described by the exponential distribution

$$f(\Lambda) = \frac{1}{\lambda_e} \exp(-\Lambda/\lambda_e) \tag{51}$$

where $\lambda_e$ is the elastic mean free path given by $\lambda_e = (N\,\sigma_t)^{-1}$, $N$ being the number of atoms per unit volume and $\sigma_t$ the total elastic cross section.

The distribution of scattering angles at the end of a linear segment is described by

$$W(\theta) = \frac{2\pi\,\sin(\theta)\,d\sigma/d\Omega}{\sigma_t} \tag{52}$$

where $d\sigma/d\Omega$ is the plane wave differential elastic scattering cross-section corresponding to scattering into a small solid angle $d\Omega$ at an angle $\theta$ with respect to the original direction.

In this framework we should therefore replace the Plane Wave DCS $d\sigma/d\Omega$ by the expression given in Eq. (50), where the distance $R_{ij}$ should be identified with the linear distance $\Lambda$ traveled by the test electron between two successive elastic scatterings. This replacement implies that $f^i_{eff}(\theta;\Lambda)$ should be recalculated at each scattering event, although $\Lambda$ can be safely replaced by an average value. The SW factor $e^{ikR_{ij}}/(kR_{ij})$ can be neglected since it does not depend on $\theta$.

As a last remark, from the way it was derived Eq. (49) clearly represents the DCS for an oriented molecule whose atoms are located at sites $\mathbf{R}_i$. Being second order in the effective scattering amplitude $f^i_{eff}(\theta;R_{ij})$ it is expected to be valid for incident electron energies above roughly 100 eV. DCS for randomly oriented molecules can be obtained by averaging Eq. (49) over all the molecular orientations. Damping effects in the electron propagation could be taken into account by the use of the complex HL potential to calculate the $t_l$-matrices.

## 3. Running details

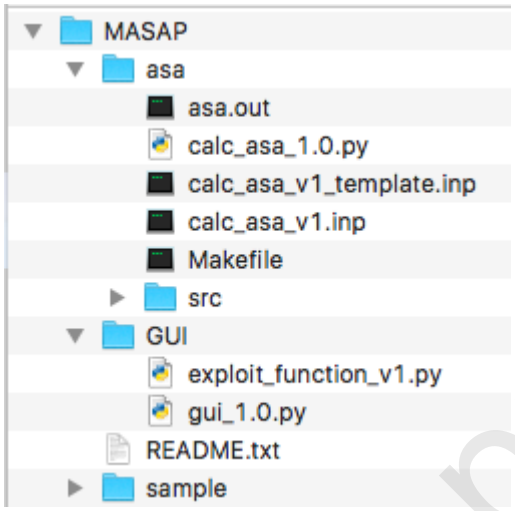


Figure 1: The directory tree of MASAP.

Figure 1 shows the directory tree of MASAP. MASAP contains the directories for the asa, GUI and sample parts. This latter part contains some outputs generated by MASAP.

The users firstly compile the source files by using Makefile and the make command in the asa directory:

```
$ make
```

The make command generates the executable asa.out, although this name can be changed, if desired, by modifying Makefile.

The users at this point can either run directly asa.out in a chosen directory, giving as input a *data.ms* file, whose template, called *template_data.ms*, can be found in the directory MASAP/asa/src and contains the explanation of all the input options, or take advantage of the graphical interface by editing the calc_asa_v1.inp file in the asa directory to enter the chosen options, and running calc_asa_1.0.py:

```
$ python calc_asa_1.0.py
```

The python script reads the corresponding inp file and runs asa.out to obtain the site $T$-matrix, which are used to calculate the ASA's. The calculated ASA's are output to HDF files in new directories whose top directory's name is designated in the inp file. The HDF files also include information on the options specified in the corresponding inp files. The typical options in the inp file are as follows:

- asaPATH: specifies the path for running the executable asa.out.
- OnlyMainFile: if "no", all the calculated results by asa.out are stored.
- NewDirName: specifies the name of the directory for the calculated ASA's.

- Potential: denotes the potential type. The real and complex Hedin-Lundqvist exc potentials are denoted by "hr" and "hc", respectively. The Dirac-Hartree-Fock potential is denoted by "fc". This potential is the same as the one used in Ref. [1] and allows the comparison of the calculated ASA's with those given in the atomic database developed by NIST [29].
- EnergyStart, EnergyEnd, EnergyInterval: specifies the range (and spacing) of the electron energies at which to calculate the ASA's.
- CheckStructure: if "yes", the input options are visualized in the pop-up windows described below.

Users define solid systems in a format accepted by the python module of Atomic Simulation Environment, and specify the target element. The calculated ASA for each described solid system is stored in separated HDF files in the directory designated by the NewDirName variable. Users can also input isolated atomic systems in calc_asa_v1.inp. For atomic systems, space groups are replaced by the keyword "atomic", and lattice constants for solid systems are replaced by the value of the atomic radii or by the keyword "calc". When this latter option is chosen, the program determines internally the atomic radius in the way specified below in Section 4. The flow-chart in Fig. 2 illustrates the various steps of the process

In the GUI directory, gui_1.0.py can plot, besides ASA's, related quantities such as cross sections, site $t_\kappa$- and $s_\kappa$-matrices and so on.

Launching the program gui_1.0.py

```
$ python gui_1.0.py
```

causes the appearance of the window shown in Fig. 3 and of another window called "Data file list" (there is no need to click the "Data file list" button). The users select in this last window one of the HDF data file created in the previous step in the directory designated by the NewDirName variable by clicking the "Add a data file" button of Fig. 3. Then they can explore all the functions listed there by clicking the corresponding check boxes. The results, like the angular dependence of the differential cross section or the energy dependence of the transport cross section are exemplified in next section . The"Bohr radius" check box toggles between Ångstrom or atomic units. The "Plot Data" button enables the instant plotting of the calculated data. By clicking the "Export Data" button a directory, whose name is related to the time and the type of the calculated data, is created in the same directory where gui_1.0py is running. Each selected calculation is written here into separated text files that are useful for plotting figures according to the chosen options.

The window "Data file list" shows paths of the selected HDF files calculated by asa.out and calc_asa_1.0.py. The content of the "Data file list" window can be edited via the "Add a data file" and "Remove selected data file" buttons situated at the bottom of the main window. The files to be removed should be selected by clicking them in the "Data file list" window before clicking the "Remove selected data file" button. Finally, the exploit_function_v1.py program has only auxiliary functions for gui_1.0.py, so that the users do not need to run it. The various steps are illustrated in the flowchart of Fig. 4.

The gross structure of the program is very simple, as can be inferred having a look at the main driving program. If the variable cluster is true, an overlapped charge density for each atom in the cluster is constructed based on the Mattheiss prescription in the subroutine *calphas*. Then atomic t-matrices, phase shifts, differential and total integrated cross sections are computed in subroutine *asa_sub* with the set of Muffin Tin radii so determined. If cluster is false, t-matrices,

phase shifts, differential and total integrated cross sections are computed in the same subroutine *asa_sub* for an isolated atom with a radius $R_s$ determined by the condition $|V(R_s)|/\epsilon \approx 10^{-5}$.

In this case only one line of coordinates is sufficient in the input file *data.ms* to specify the symbol and the atomic number of the atom in question. The atomic charge density is calculated in the subroutine *scfdat* [17],

In the present version the program runs up to an energy of about 15 Kev. To increase further this range the user should modify the parameters *dpas* of the linear-log mesh in the subroutine *llmesh* in order to have more points in the final part of the integration range of the radial solution of the pseudo-Schrödinger equation, otherwise the program is unable to calculate the atomic matrices $t_l$ for high $l$. The variable $dpas = d\tilde{\rho}$ is the constant spacing of the Numerov integration procedure which, due to the relation $\tilde{\rho} = \alpha r + \beta \log(r)$, represents also the spacing of the radial variable $r$, when this is greater than one. In the present version $dpas = 0.01$ and should be decreased if needed.

## 4. Typical results

In this section, we show calculated DCS and $\sigma^{tr}$ in isolated atomic systems and in solids. aluminum and gold are chosen as typical light and heavy elements having FCC crystal structure. The lattice constants of FCC aluminum and gold are 4.05 and 4.07 Å, respectively, resulting in an atomic MT radius of about 1.43 Å [30, 31].

For each element we construct three kinds of atomic potentials. The first one, referred to as "solid", is a truncated-overlapped potential of the MT type, constructed according to the Mattheiss prescription [9], representing the potential of an atom embedded in a cluster, that can be chosen by the user. The second one, referred to as "input", is the potential of an isolated atom constructed on the basis of its self-consistent charge density, truncated at the same MT radius of the "solid" calculation. The label "input" refers to the fact that the MT radius is provided in the input data file. The third one, referred to as "calc", is the potential of an isolated atom, truncated at a radius $R_s$ determined such that $|V(R_s)|/\epsilon \approx 10^{-5}$, as anticipated above in section 2.1. Since the potential decays exponentially for a neutral atom, it is expected that the calculated DCS is insensitive to this truncation radius, which turns out to be of the order of about 5 to 15 a.u., depending on the element and the incident electron energy. Therefore, comparison of DCS calculations between the "solid" and "input" conditions gives information of the effects of the electron density in solids, comparison between the "input" and "calc" conditions gives information of the effects of the truncation of the atomic potential, and comparison between the "solid" and "calc" conditions gives information both on the truncation and the solid effects.

As anticipated, the real and complex Hedin-Lundqvist potentials are denoted "hr" and "hc", respectively, and the exchange part of the DHF potential in Ref. [1], used also in Ref. [2], is denoted as "fc". The non-relativistic and scalar-relativistic approximations are denoted as "nr" and "sr", respectively, whereas the use of the full relativistic potential with spin-orbit part is denoted "so". Not to clutter the figures, we have drawn only the "nr" and "so" options, although, if needed, the user can also choose the "sr" option in the program. The notation "NIST" indicates the DCS obtained from the database by NIST [29] and corresponds to our "calc" with "so" and "fc" options. For sake of comparison it is also shown in the 'solid" and "input" options.

Figures 5-8 show calculated DCSs for aluminum and gold at impinging electron energies of 100 and 1000 eV. Each figure compares calculated DCSs for the different types of potentials in non-relativistic ("nr") and full relativistic ("so") options. We see that our calculated DCS's with

the "fc" potential in the "calc" and "so" options reproduce rather well the DCS's taken from the NIST database [29], as calculated in Ref. [1].

A point worth of further investigation is the following. In the "solid" condition for aluminum with the electron energy of 100 eV, the DCS's calculated with the "hc" potential are closer to the NIST one than those with the "hr" potential (see Fig. 5). Similarly, in the "solid" condition for gold with the "so" potential, the DCS with the "hc" potential shows agreement with the NIST ones (Figs. 7 and 8). This observation seem to indicate that damping effects by the imaginary part of optical potential play some role in the connection between DCS with an effective atomic radius in a solid and purely atomic DCS. So far, the atomic DCS (or ASA) databases have been used to analyze electron scattering phenomena even in solids [1]. Tanuma et al. reported that, according with the Bethe theory, damping effects in solids are less important than in atomic systems [32]. This justifies the use of the atomic DCS (or ASA) without inelastic scattering for studying solid systems. However, Bethe's theory is valid in the electron-energy range higher than about 1 keV. Thus, our results seem to suggest that damping effects make the DCS in solids approximately similar to the atomic DCS, which justifies the use of the atomic DCS (or ASA) database to analyze electron scattering phenomena in solid systems also at electron energies less than 1 keV. Note that for high electron energy, the potential differences become less pronounced, and thus the DCS's for aluminum with the electron energy of 1000 eV are relatively similar (Fig. 6) On the other hand, because heavy element atoms have strong Coulomb attractive potential near the nucleus, relatively larger difference between the DCS's calculated with the various potentials appears for gold in Fig. 8 than for aluminum in Fig. 6.

Moreover, a look at the various figures shows that the difference of DCS between the "solid" and "input" conditions is smaller than that between the "input" and "calc" conditions. This fact indicates that the difference in electron density generated by the overlapping mechanism is less important than the truncation of the potential effective radius, for electron energies roughly higher than 100 eV. Therefore the description of electron scattering in a solid requires a truncated potential.

Since the idea behind the present paper is the investigation of the validity and limitations of the HL potential, it is useful to restrict the application of the program to the somewhat low-energy range of 50: ≈1500 eV. This is also the range used in EXAFS (Extended X-ray Absorption Fine Structure) structural analysis, which is known to be sensitive to the details of the atomic potential. In fact, at higher energies, the scattering process progressively becomes insensitive to the details of the scattering potential. The hope is that the study of atomic DCS's will bring new information compared to EXAFS structural analysis.

In order to have an idea of the difference between the HL and Furness-McCarthy potentials, Fig. 9 plots the real (*vxcrl*) and the imaginary part (*vxcim*) of the HL potential versus the Furness-McCarthy exchange ($vx\_fc$) and X-alpha ($v\_xa$) potentials as a function of the radial distance from the origin of the Krypton atom at 100 eV of electron energy. Notice that the imaginary part *vxcim* has been mutliplied by ten to be visible on the same scale. Their mutual relation is a representative case of a general behavior for atomic potentials. Near the origin *vxcrl* and $v\_xa$ have a value of 75.7 Ryd whereas at great distances *vxcrl* decays much more rapidly than $v\_xa$ (for example at 11 a.u. $vxcrl = 4.3E(-05)$ compared to $v\_xa = 2.4E(-3)$). This behavior affects the corresponding DCS's values in the forward direction, in the sense that higher values of the exchange potential correspond to higher cross sections.

The upper panel of Fig. 10 illustrates this behavior in the case of Al at 1Kev of incident energy without polarization potential, whereas the lower panel plots the same comparison in the presence of a polarization potential. As expected the polarization potential increases the DCS's

value in the forward direction. The curve for X-alpha potential is not shown because it would be out of scale toward much higher DCS's values.

A point worth mentioning is that the imaginary part of the optical potential enhances the calculated elastic DCSs in the forward direction compared to the same potential without the imaginary part, but gives rise to a lower intensity at all other directions as expected from the damping effect of the complex part of the potential. The forward direction effect is related to the optical theorem (21), because, in the presence of an absorptive part, $\Im f_k(0)$ has a contribution coming from all inelastic processes, so that $|f_k(0)|^2 = |\Re f_k(0)|^2 + |\Im f_k(0)|^2$ is enhanced.

Generally, relativistic effects are not important for light elements. For them, relativistic ("so", "sr") and non relativistic ("nr") DCS's superimpose for all kinds of potentials. For heavy elements instead there is almost coincidence in a wide forward cone of about 30-40 degrees, after which the DCS's begin to differ, the more so the lower the energy. This finding can be explained on the basis that the tail of the scattering potential contributes to the forward scattering, whereas its interior determines the large angle scattering.

The role of the complex potential is illustrated in Fig. 11 where the DCS for the noble gas Krypton at the impinging electron energy of 100 eV, calculated with the complex exchange-correlation potential HL, labeled "hc", is compared with the DCS calculated with the same potential but without imaginary part, labeled "hr", and the real DHF potential used in Ref. [1], denoted "fc". All calculations are done in the fully relativistic "so" mode, including therefore the spin-orbit potential. The experimental results are taken from Ref.s [33] (symbol *), [34] (symbol #) and [35] (symbol $). Notice that in the range 40-120 degrees the data from Ref.s [34, 35] are almost coincident. The green curve represent the results calculated using the (non relativistic) R-matrix method by Fon *et al* [36]. It should be compared with the curve labeled "hr", which does not differ significantly by the same curve calculated in non-relativistic mode as already noted.

The comparison wih the experimental data reveals the need to include an absorptive part in the scattering potential to describe the whole scattering angular range. There is however a discrepancy between calculated (198 $a_0^2\,\mathrm{sr}^{-1}$) and experimental (136 $a_0^2\,\mathrm{sr}^{-1}$) forward cross sections, indicating that the imaginary part of the HL potential is a bit overestimated.

It is also interesting to plot Krypton DCS spectra at 1, 2 and 3 Kev of impinging electron energy against the experimental available data from [37]. The agreement is very good, as shown in Fig. 12. Our calculations compare very well with those of Salvat in Ref. [3].

The comparison with the spectra at 100 eV and those at 1, 2 and 3 Kev confirms the fact that the higher the electron impinging energy, the lower the discrimination power with respect to the details of the atomic potential. The upper panel of Fig. 13 illustrates this fact. At 1 KeV of incident energy the Krypton DCS's corresponding to the "hr" and "fc" potentials are almost identical, except in the forward direction, whereas the complex "hc" potential has still a noticeable effect. Even this difference however decreases with increasing electron energy , as shown in the middle panel of the same figure, which shows the same comparison at 3KeV. As another example, the lower panel of Fig. 13 plots the DCS corresponding to three types of potential in the case of Gold at 10 Kev of incident electron energy. The curves are almost coincident and in good agreement with the same calculation shown in Fig. 6 of Ref. [1], indicating that at this energy the scattering process is insensitive to the exchange and complex part of the potential. The same is found for Krypton at 10 KeV.

The favorable situation for the complex "hc" potential found in Krypton is not met in the case of Argon at 100 eV of incident energy. Fig. 14 compares in the upper panel the DCS's for Argon at 100 eV of impinging electron energy, in the "calc" mode with "so" option for "hr", "hc"

potentials. The experimental points are derived from [38] (symbol #). The red curve, labeled "R-matrix', represent the results for the DCS calculated using the R-matrix method (non-relativistic) by Fon *et al* [39]. It seems that the complex potential overdamps the spectral features and that a description in terms of a real potential, at least in parts of the angular spectrum, would be more appropriate (see the R-matrix spectrum). Another calculation with the complex part of the potential reduced uniformly by the factor 0.7 reported in the lower panel of Fig. 14 shows a better agreement with the data.

With our surprise the experimental spectrum at 300 eV is instead reproduced quite well by the use of the complex ("hc") potential, as shown in Fig. 15. Here the experimental points are derived from [40] (symbol #) and [41] (symbol $). This finding seems to point out to an incorrect energy dependence of the complex part of the HL potential, already pointed out at by other authors [23, 24].

The quality of the energy dependence of the HL is illustrated in Fig. 16 where the integrated total and elastic cross sections, derived from the DCS's for the "hc-so" potential (no reduction of the imaginary part) is compared with experimental data and R-matrix calculations. In both cases the total calculated CS is roughly 50-100% higher than the experimental counterpart, whereas the the disagreement is less for the elasic CS. In the case of Argon the total and elastic CS cross at 30 eV, indicating an inconsistency of the data or an high threshold for the opening of the inelastic channels. Further investigation would be desirable.

Finally the upper panel of Fig. 17 compares the DCS's for Mercury at 35 eV of incident energy, in the "calc" mode with "so" option for "hc" and "hr" potentials with the relativistic R-matrix calculations [42] (experimental data taken from Ref. [43]). As stated in Ref. [42] the good agreement of the R-matrix calculations "suggests that channel coupling and relativistic effects are not particularly important for these cases (25 and 35 eV). At these energies, it has essentially become a potential-scattering problem, with the accuracy of the scattering potential being the decisive element that determines success or failure of a theoretical approach". This observation explains also the relatively good agreement with the "hc" calculation, apart the slight overdamping. Again, a reduction by a factor 0.7 of the imaginary part of the "hc" potential improves decidedly the agreement both with the R-matrix approach and the experimental data, as shown in the lower panel of Fig. 17. Fig. 18 compares instead the relativistic and non relativistic DCS's for the "hc" potential, which seems to confirm the conjecture made in Ref. [42]. Notice however the disagreement in the forward 20 degrees cone, even with the "hr" type of potential, a situation also observed in the case of Krypton at 100 eV (see Fig. 11). This disagreement can be explained on the basis that the GW local density approximation for the self-energy, assumed in the HL exchange-correlation potential, is not justified when the electron density is very low, as in the tail of the atomic density.

All in all, we think that the whole matter deserves a more exhaustive analysis, which will be given elsewhere. These preliminary results seem to indicate that the process of electron-atom scattering is complementary to structural EXAFS analysis.

Fig. 19 compares the DCS's calculated using plane wave (pw) and spherical wave (sw) propagators (Eq. (50)) in the case of Aluminum at 100 eV of electron energy, in the "solid" mode with "sr" and "hc" options. Usually the effect of the spherical wave correction on the TCS $\sigma^{tr}$ is a rough average increase of 25 % with respect to the plane wave calculation in the whole 50-1000 eV range of Aluminum and Gold.

The effect of the presence of a polarization potential is illustrated in Fig. 20. We again consider a Krypton atom scattering an electron beam of 10 eV. The potential parameters defined in Eq. (42) are taken as $\alpha_0 = 16.7$ au from Ref. [44] and $d = 1.66$ a.u. equal to the atomic

radius. This value is in keeping with the empirical formula suggested in Eq. (5) of Ref. [3]. Calculations have been done in the "calc" mode with "hc" and "so" options. Fig. 20 compares in the upper panel the DCS in presence (labeled "hc-wpl") and in absence (labeled "hc-npl") of the polarization potential. The lower panel shows the same comparison at an impinging electron energy of 100 eV. The effect of the polarization potential on the DCS is much less pronounced. However, remembering Fig. 10, this is not a general rule.

Finally Figures 21 and 22 show the calculated $\sigma^{tr}$ and the NIST one. Data are presented with an energy mesh of 50 eV, but users can choose their own mesh. We can observe that $\sigma^{tr}$ with the "hc" potential is smaller than that with the "hr" potential, which agrees with the physical intuition of the damping effects by the imaginary part of the optical potential. As in the case of the calculated DCS, $\sigma^{tr}$ calculated with the "hc" potential in the "solid" mode agrees with the NIST one, which again justifies the use of the atomic CS without the damping effects for analyzing electron scattering phenomena in solids. Comparison between $\sigma^{tr}$ in the "input" and "calc" mode shows that $\sigma^{tr}$ calculated with the "hc" potential is sensitive to the atomic radius for electron energies less than 200 eV, but $\sigma^{tr}$ calculated with the real potentials "hr" and "fc" are not, which indicates that the imaginary part of the "hc" potential has more contribution in outer region within the atomic sphere than the real potentials. Note that $\sigma^{tr}$ is less sensitive to the forward scattering due to the factor $(1 - \cos\theta)$ in Eq. (19).

## 5. Summary

The computational MASAP Package, composed of a computation program and a graphical interface, generates atomic scattering amplitude of an atom, either isolated or embedded in an environment, at any chosen energy of the impinging electron up to 15 KeV. The ASA is calculated using an effective, complex optical potential which provides damping effects in the scattering process in a fully relativistic framework. Optionally, scalar relativistic and non-relativistic approximations are also available to assess their applicability to a given problem.

The GUI part allows to output quantities related ASA with user selected options into text files for convenient plotting.

For sake of illustration, we have calculated the differential and transport CS's for aluminum and gold in isolated atomic systems and in solids. The comparison of the various DCS's suggest that the use of complex potential at impinging electron energy less than 1 keV justifies the approximate application of the atomic databases DCS's, based on free atom potential, to electron scattering phenomena in solid systems. Instead, the description of the free atom Differential Cross Section has been shown to require the use of a complex potential in the whole angular scattering range, confirming the conclusions of Ref. [3]. The preliminary analysis carried out on selected examples seems to indicate that the process of electron-atom scattering is complementary to structural EXAFS analysis in providing information on the scattering potential.

Finally, taking inspiration from Multiple Scattering Theory for the description of electron propagation in solids, an effective scattering amplitude has been suggested, to be used in Monte Carlo simulations and electron-molecule scattering, based on spherical wave propagators and MT atomic embedded potentials constructed according to the Mattheiss prescription [9].

## 6. Acknowledgment

The research leading to these results has received funding from the People Programme (Marie Curie Actions) of the European Union's Seventh Framework Programme (FP7/2007-2013) un-

der REA grant agreement n. PCOFUND-GA-2013-60912, through the PRESTIGE programme (PRESTIGE-2017-2-0016) coordinated by Campus France.

## References


[1] A. Jablonski, F. Slavat, C. J. Powell, Comparison of electron elastic-scattering cross sections calculated from two commonly used atomic potentials, J. Phys. Chem. Ref. Data. 33 (2004) 409.

[2] F. Salvat, A. Jablonski, C. J. Powell, ELSEPA - Dirac partial-wave calculation of elastic scattering of electrons and positrons by atoms, positive ions and molecules, Computer Physics Communications 165 (2) (2005) 157–190. doi:https://doi.org/10.1016/j.cpc.2004.09.006.
URL https://www.sciencedirect.com/science/article/pii/S0010465504004795

[3] F. Salvat, Optical-model potential for electron and positron elastic scattering by atoms, Phys. Rev. A 68 (2003) 012708. doi:10.1103/PhysRevA.68.012708.
URL https://link.aps.org/doi/10.1103/PhysRevA.68.012708

[4] L. Hedin, New method for calculating the one-particle green's function with application to the electron-gas problem, Phys. Rev. 139 (1965) A796–A823.

[5] L. Hedin, S. Lundqvist, Solid State Phys. 23 (1970) 33.

[6] A. Ankudinov, B. Ravel, J. J. Rehr, S. Conradson, Real-space multiple-scattering calculations and interpretation of x-ray absoprtion near-edge structure, Phys. Rev. B 58 (1998) 7565–7575.

[7] A. Filipponi, A. Di Cicco, C. R. Natoli, X-ray absorption spectroscopy and n-body distribution functions in condensed matter (I): theory., Phys. Rev. B 52 (1995) 15122–15134.

[8] C. Fadley, S. Thevuthasan, A. Kaduwela, C. Westphal, Y. Kim, R. Ynzunza, P. Len, E. Tober, F. Zhang, Z. Wang, S. Ruebush, A. Budge, M. V. Hove, Photoelectron diffraction and holography: Present status and future prospects, Journal of Electron Spectroscopy and Related Phenomena 68 (1994) 19 – 47. doi:https://doi.org/10.1016/0368-2048(94)02101-5.

[9] L. F. Mattheiss, Energy bands for solid argon, Phys. Rev. 133 (1964) A1399–A1403.
URL https://link.aps.org/doi/10.1103/PhysRev.133.A1399

[10] C. R. Natoli, D. Sébilleau, Springer Proceedings in Physics, Multiple Scattering Theory for Spectroscopies: D. Sébilleau and K. Hatada and H. Ebert editors Edition, Vol. 204, Springer International Publishing, 2018, Ch. Generating Phase-Shifts and Radial Integrals for Multiple Scattering Codes, pp. 35–65.

[11] M. Rose, Relativistic Electron Theory, Wiley, 1961.
URL https://books.google.it/books?id=gh5RAAAAMAAJ

[12] J. H. Wood, A. M. Boring, Improved Pauli hamiltonian for local-potential problems, Phys. Rev. B 18 (1978) 2701–2711.
URL https://link.aps.org/doi/10.1103/PhysRevB.18.2701

[13] C. E. Theodosiou, Lifetimes of alkali-metal—atom rydberg states, Phys. Rev. A 30 (1984) 2881–2909.
URL https://link.aps.org/doi/10.1103/PhysRevA.30.2881

[14] M. Y. Amusia, L. V. Chernysheva, Computation of Atomic Processes, IOP publishing, London, 1997.

[15] D. Walker, Relativistic effects in low energy electron scattering from atoms, Advances in Physics 20 (85) (1971) 257–323.
URL https://doi.org/10.1080/00018737100101251

[16] N. Mott, The scattering of fast electrons by atomic nuclei, Proc. R. Soc. Lond. A 124 (1929) 425–442.
URL https://doi.org/10.1098/rspa.1929.0127

[17] A. Ankudinov, S. Zabinsky, J. Rehr, Single configuration dirac-fock atom code, Computer Physics Communications 98 (3) (1996) 359–364. doi:https://doi.org/10.1016/0010-4655(96)00097-5.

[18] C. R. Natoli, M. Benfatto, S. D. Longa, K. Hatada, X-ray absorption spectroscopy: state-of-the-art analysis, J. Synchrotron Rad. 10 (2003) 26–42.

[19] J. M. de Leon, J. J. Rehr, S. I. Zabinsky, R. C. Albers, *Ab initio* curved-wave x-ray-absorption fine structure, Phys. Rev. B 44 (1991) 4146.

[20] D. Sebilleau, R. Gunnella, Z.-Y. Wu, S. D. Matteo, C. R. Natoli, Multiple-scattering approach with complex potential in the interpretation of electron and photon spectroscopies, J. Phys.: Cond. Matter 18 (2006) R175–R230.

[21] D. R. Penn, Electron mean-free-path calculations using a model dielectric function, Phys. Rev. B 35 (1987) 482–486. doi:10.1103/PhysRevB.35.482.
URL https://link.aps.org/doi/10.1103/PhysRevB.35.482

[22] P. A. Lee, G. Beni, New method for the calculation of an atomic phase shifts: Application to extended x-ray absorption fine structure (EXAFS) in molecules and crystals, Phys. Rev. B 15 (1977) 2862–2883.

[23] J. J. Kas, A. P. Sorini, M. P. Prange, L. W. Cambell, J. A. Soininen, J. J. Rehr, Many-pole model of inelastic losses in x-ray absorption spectra, Phys. Rev. B 76 (2007) 195116. doi:10.1103/PhysRevB.76.195116.
URL https://link.aps.org/doi/10.1103/PhysRevB.76.195116

[24] J. J. Rehr, J. J. Kas, M. P. Prange, A. P. Sorini, Y. Takimoto, F. Vila, Ab initio theory and calculations of x-ray spectra, Comptes Rendus Physique 10 (6) (2009) 548–559, theoretical spectroscopy. doi:https://doi.org/10.1016/j.crhy.2008.08.004.
URL https://www.sciencedirect.com/science/article/pii/S1631070508001084

[25] B. Bransden, C. Joachain, Physics of Atoms and Molecules, 2014.

[26] J. J. Rehr, R. C. Albers, C. R. Natoli, E. A. Stern, New high-energy approximation for x-ray-absorption near-edge structure, Phys. Rev. B 34 (1986) 4350–4353.
URL https://link.aps.org/doi/10.1103/PhysRevB.34.4350

[27] A. Jablonski, P. Jiricek, Dependence of experimentally determined inelastic mean free paths of electrons on the measurement geometry, Surface Science 412-413 (1998) 42–54. doi:https://doi.org/10.1016/S0039-6028(98)00367-7.
URL https://www.sciencedirect.com/science/article/pii/S0039602898003677

[28] A. Jablonski, Determination of the IMFP from electron elastic backscattering probability, Surface and Interface Analysis 29 (9) (2000) 582–595. doi:https://doi.org/10.1002/1096-9918(200009)29:9¡582::AID-SIA903¿3.0.CO;2-X.

[29] A. Jablonski, F. Salvat, C. J. Powell, A. Y. Lee, NIST Electron Elastic-Scattering Cross-Section Database Version 4.0, NIST Standard Reference Database Number 64, National Institute of Standards and Technology, Gaithersburg MD, 20899 (2016) 1043Https://srdata.nist.gov/srd64/, (retrived 15/02/2019).

[30] S. Popović, B. Gržeta, V. Ilakovac, R. Kroggel, G. Wendrock, H. Löffler, Phys. Status Solidi A 130 (1992) 273.

[31] W. S. Jr., B. Lalevic, N. Fuschillo, J. Appl. Phys. 44 (1973) 2891.

[32] S. Tanuma, C. J. Powell, D. R. Penn, Surf. Interface Anal. 25 (1997) 25.

[33] R. W. Wagenaar, A. de Boer, T. van Tubergen, J. Los, F. J. de Heer, Absolute differential cross sections for elastic scattering of electrons over small angles from noble-gas atoms, Journal of Physics B: Atomic and Molecular Physics 19 (19) (1986) 3121. doi:10.1088/0022-3700/19/19/024.
URL https://dx.doi.org/10.1088/0022-3700/19/19/024

[34] A. Danjo, Electron scattering from kr. i. differential cross section for elastic scattering, Journal of Physics B: Atomic, Molecular and Optical Physics 21 (22) (1988) 3759. doi:10.1088/0953-4075/21/22/014.
URL https://dx.doi.org/10.1088/0953-4075/21/22/014

[35] D. Cvejanovic, A. Crowe, Differential cross sections for elastic scattering of electrons from argon and krypton as a continuous function of energy, Journal of Physics B: Atomic, Molecular and Optical Physics 30 (12) (1997) 2873. doi:10.1088/0953-4075/30/12/016.
URL https://dx.doi.org/10.1088/0953-4075/30/12/016

[36] W. C. Fon, K. A. Berrington, A. Hibbert, The elastic scattering of electrons from inert gases. iv. krypton, Journal of Physics B: Atomic and Molecular Physics 17 (16) (1984) 3279. doi:10.1088/0022-3700/17/16/011.
URL https://dx.doi.org/10.1088/0022-3700/17/16/011

[37] R. H. J. Jansen, F. J. de Heer, Absolute differential cross sections for elastic scattering of electrons by krypton and xenon, Journal of Physics B: Atomic and Molecular Physics 9 (2) (1976) 213. doi:10.1088/0022-3700/9/2/010.
URL https://dx.doi.org/10.1088/0022-3700/9/2/010

[38] L. Vuskovic, M. V. Kurepa, Differential cross sections of 60-150 ev electrons elastically scattered in argon, Journal of Physics B: Atomic and Molecular Physics 9 (5) (1976) 837. doi:10.1088/0022-3700/9/5/026.
URL https://dx.doi.org/10.1088/0022-3700/9/5/026

[39] W. C. Fon, K. A. Berrington, P. G. Burke, A. Hibbert, The elastic scattering of electrons from inert gases. iii. argon, Journal of Physics B: Atomic and Molecular Physics 16 (2) (1983) 307. doi:10.1088/0022-3700/16/2/018.
URL https://dx.doi.org/10.1088/0022-3700/16/2/018

[40] J. F. Williams, B. A. Willis, The scattering of electrons from inert gases. i. absolute differential elastic cross sections for argon atoms, Journal of Physics B: Atomic and Molecular Physics 8 (10) (1975) 1670. doi:10.1088/0022-3700/8/10/017.
URL https://dx.doi.org/10.1088/0022-3700/8/10/017

[41] R. H. J. Jansen, F. J. de Heer, H. J. Luyken, B. van Wingerden, H. J. Blaauw, Absolute differential cross sections for elastic scattering of electrons by helium, neon, argon and molecular nitrogen, Journal of Physics B: Atomic and Molecular Physics 9 (2) (1976) 185. doi:10.1088/0022-3700/9/2/009.
URL https://dx.doi.org/10.1088/0022-3700/9/2/009

[42] O. Zatsarinny, K. Bartschat, Fully relativistic *b*-spline *r*-matrix calculations for electron collisions with mercury, Phys. Rev. A 79 (2009) 042713. doi:10.1103/PhysRevA.79.042713.
URL https://link.aps.org/doi/10.1103/PhysRevA.79.042713

[43] G. Holtkamp, K. Jost, F. J. Peitzmann, J. Kessler, Absolute differential cross sections for elastic electron scattering

from mercury, Journal of Physics B: Atomic and Molecular Physics 20 (17) (1987) 4543. doi:10.1088/0022-3700/20/17/030.
URL https://dx.doi.org/10.1088/0022-3700/20/17/030

[44] P. Schwerdtfeger, J. K. Nagle, 2018 Table of static dipole polarizabilities of the neutral elements in the periodic table, Molecular Physics 117 (9-12) (2019) 1200–1225.
URL https://doi.org/10.1080/00268976.2018.1535143

[45] R. W. Wagenaar, F. J. de Heer, Total cross sections for electron scattering from ar, kr and xe, Journal of Physics B: Atomic and Molecular Physics 18 (10) (1985) 2021. doi:10.1088/0022-3700/18/10/017.
URL https://dx.doi.org/10.1088/0022-3700/18/10/017

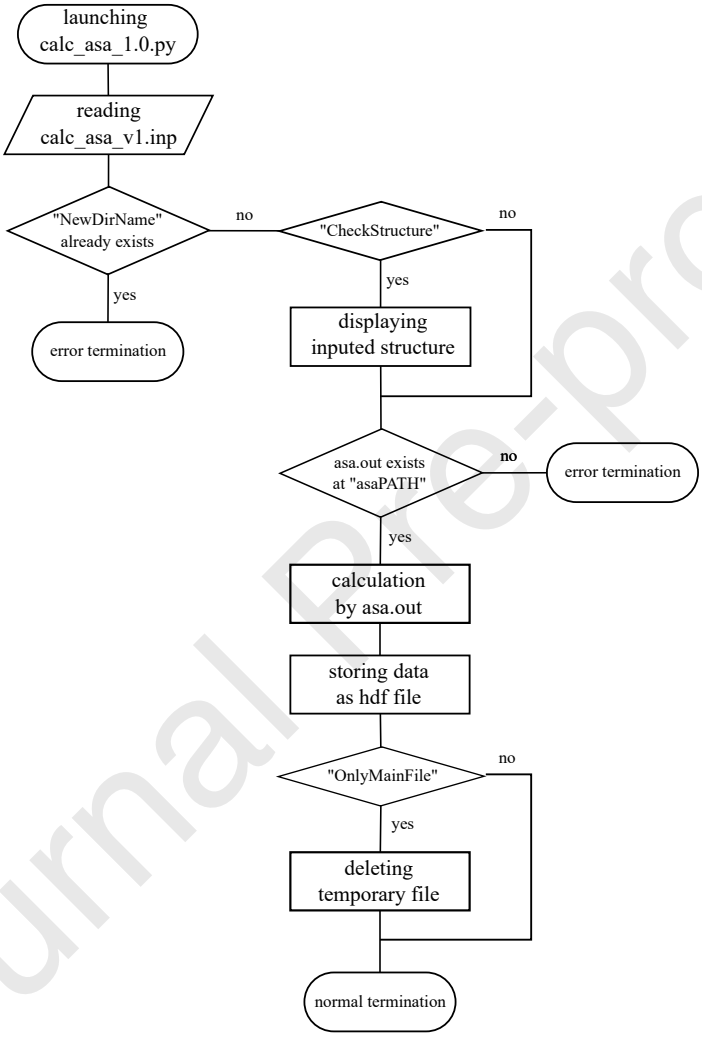


Figure 2: The calc_asa flowchart

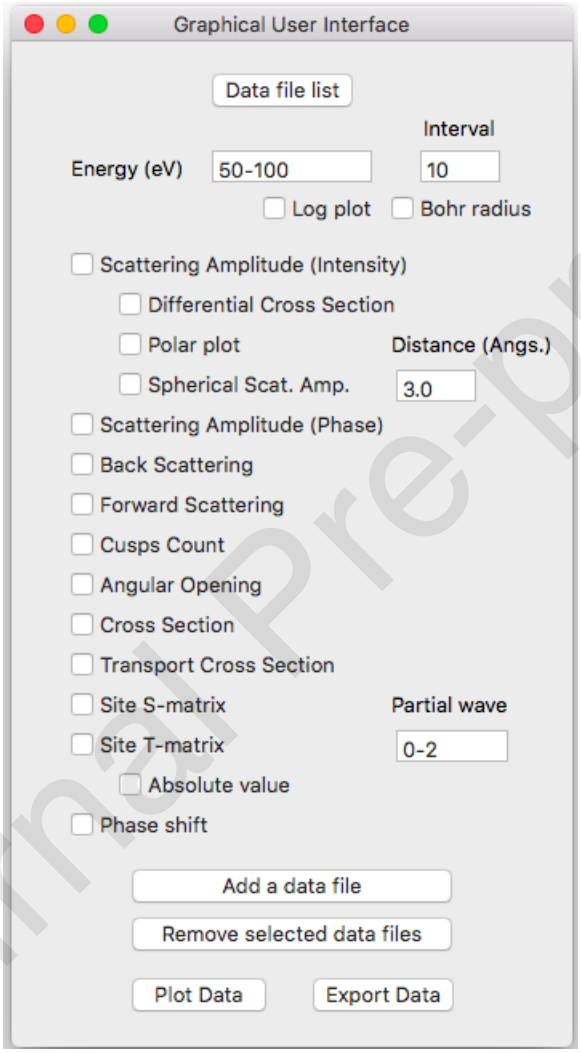


Figure 3: The main window of gui_1.0.py.

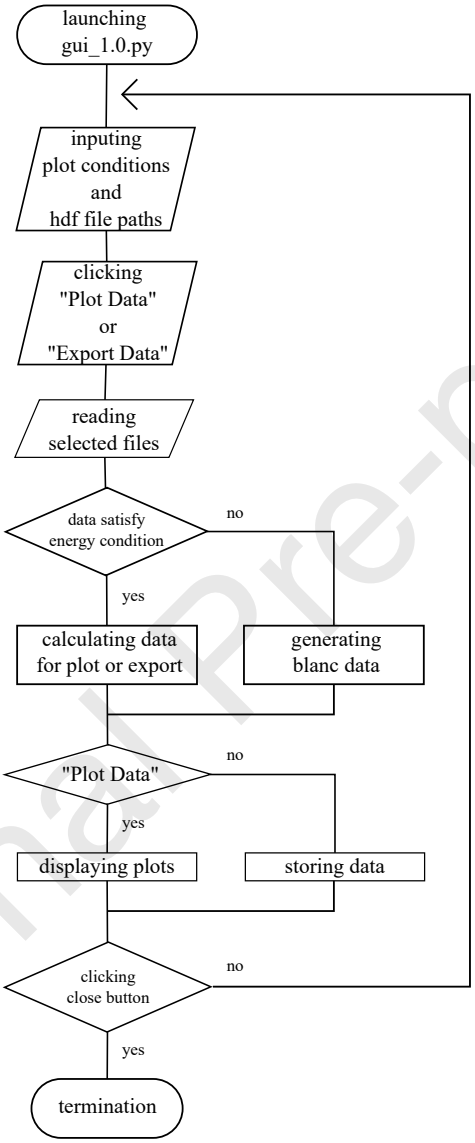


Figure 4: The GUI flowchart

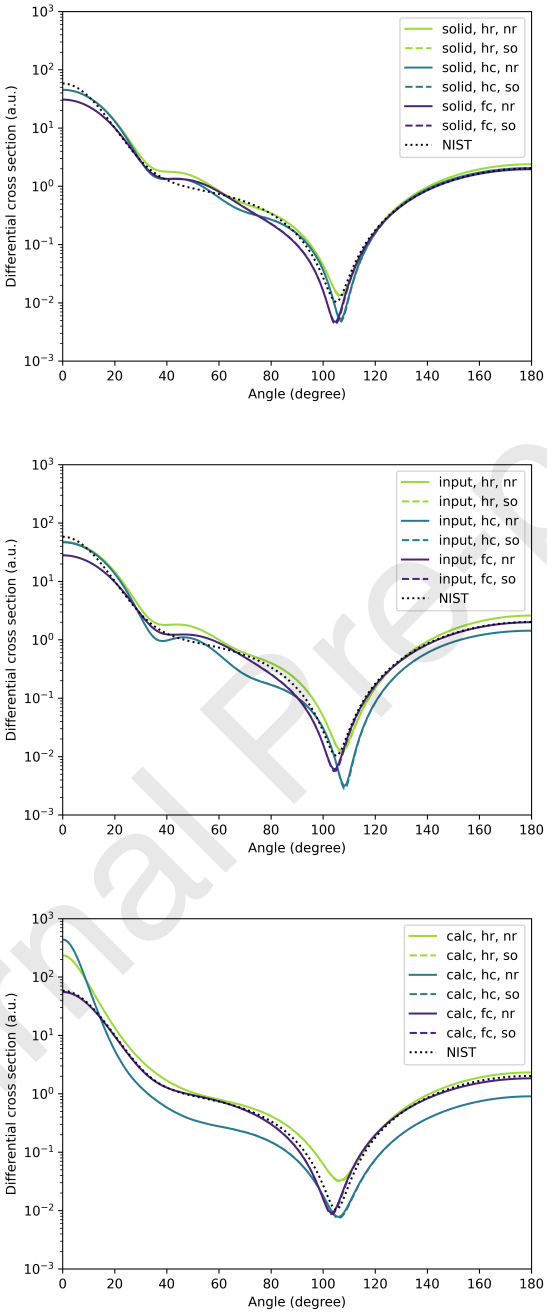


Figure 5: Calculated DCS for aluminum at impinging electron energy of 100 eV. See text (Section 4) for the meaning of the various labels.

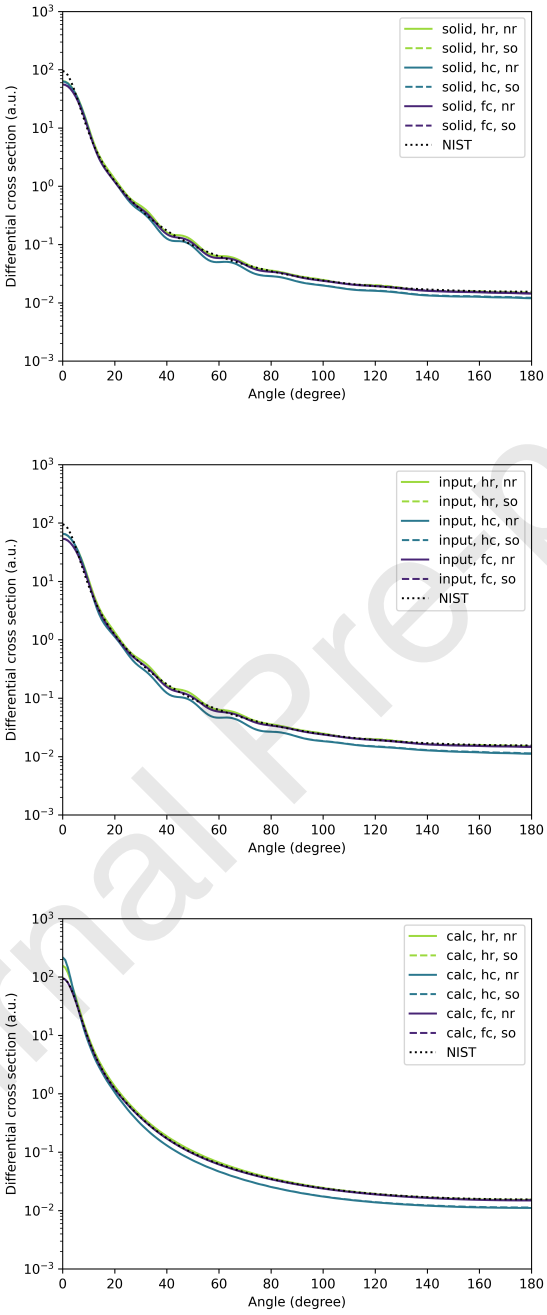


Figure 6: Calculated DCS for aluminum at impinging electron energy of 1000 eV. See text (Section 4) for the meaning of the various labels.

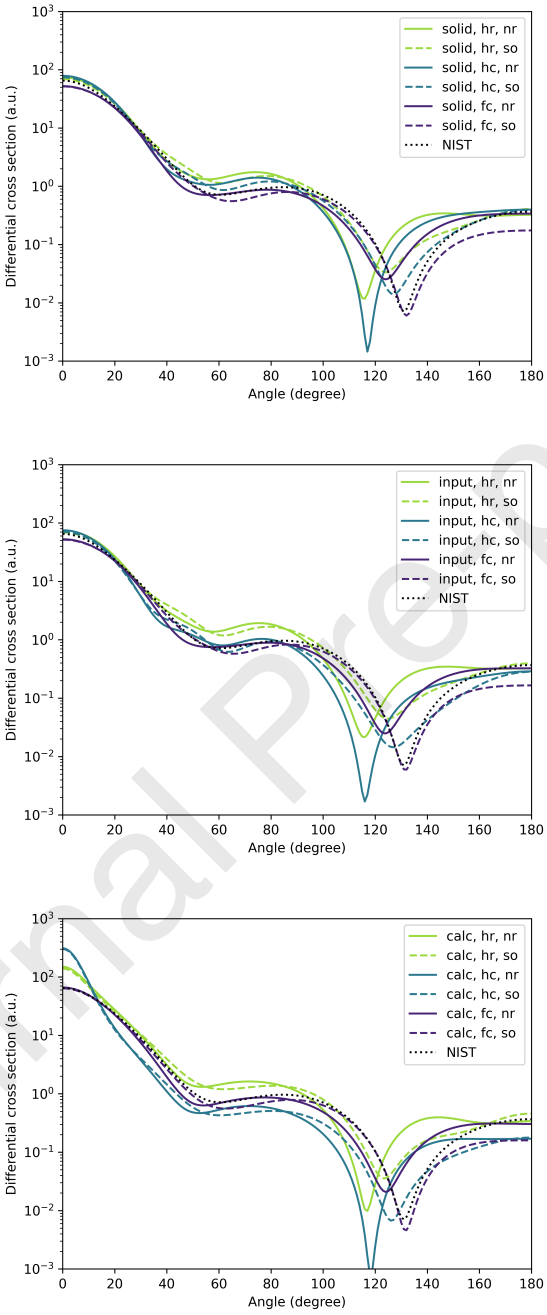


Figure 7: Calculated DCS for gold at impinging electron energy of 100 eV. See text (Section 4) for the meaning of the various labels.

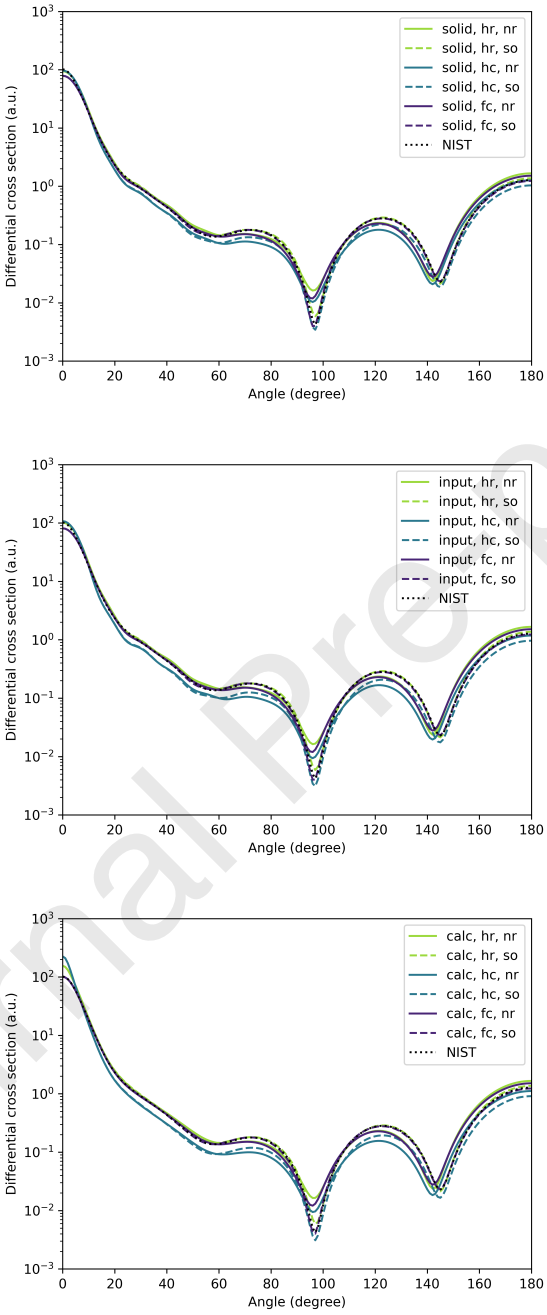


Figure 8: Calculated DCS for gold at impinging electron energy of 1000 eV. See text (Section 4) for the meaning of the various labels.

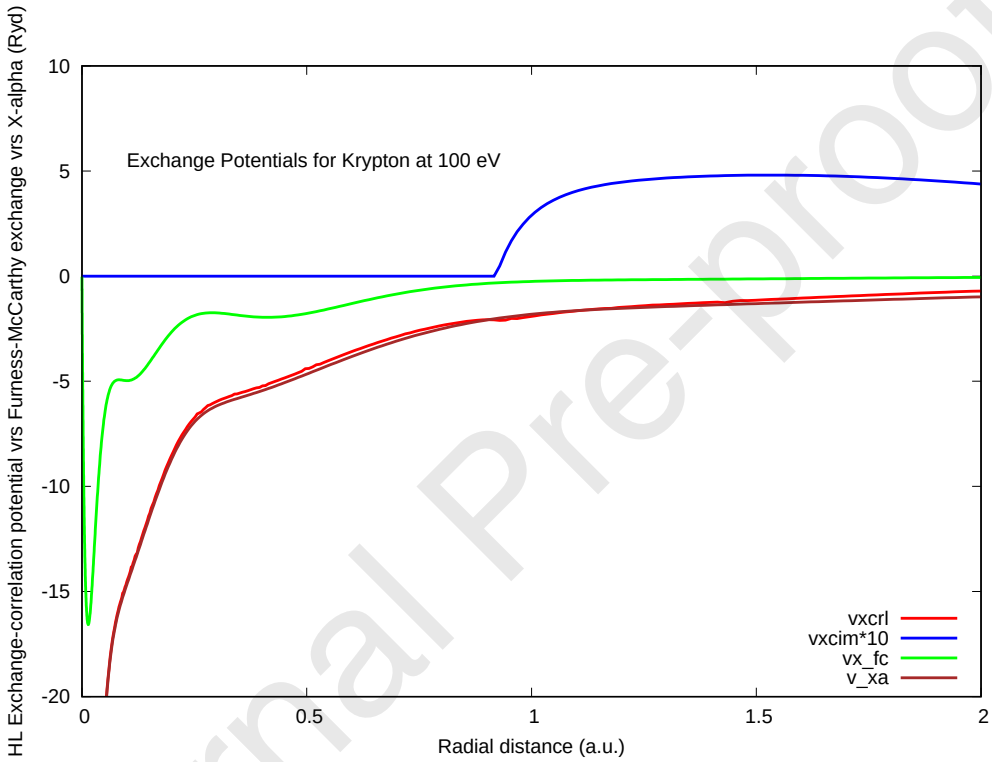


Figure 9: Plot of the real (vxcrl) and imaginary part (*vxcim*) of the HL potential versus the Furness-McCarthy exchange (vx_fc) and X-alpha (v_xa) potenials as a function of the radial distance from the origin of the Krypton atom at 100 eV of incident electron energy. Notice that the imaginary part *vxcim* has been mutliplied by 10 to be visible on the same scale.

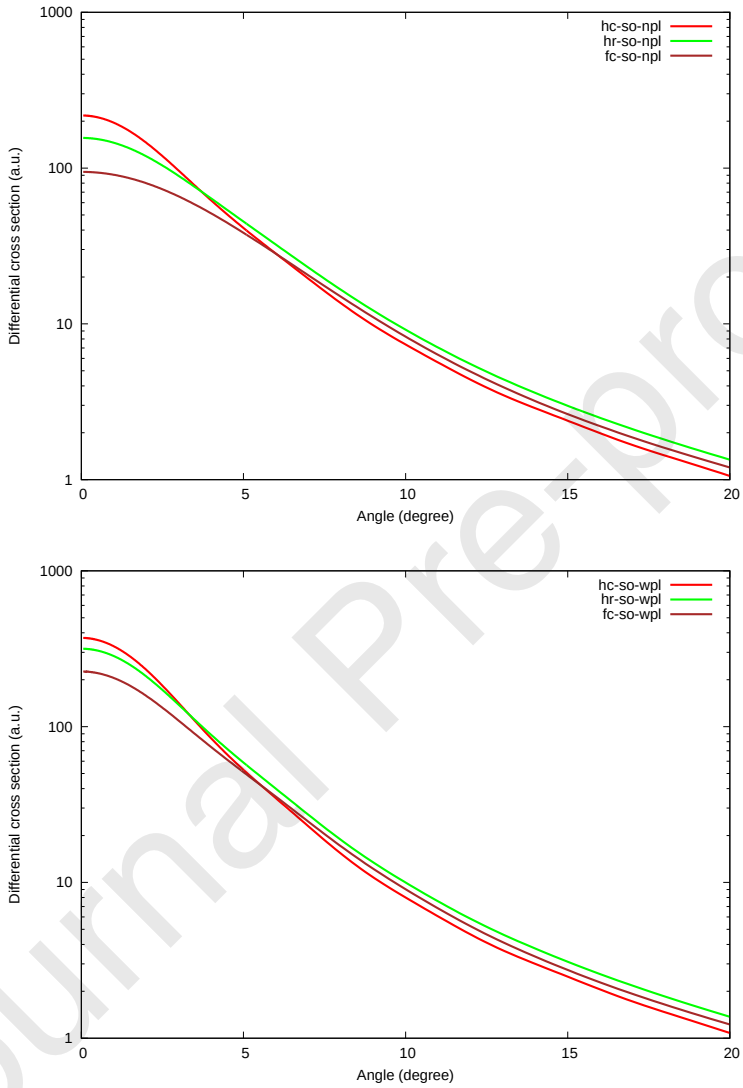


Figure 10: Upper panel: Comparison between DCS's for Aluminum at 1KeV eV of impinging electron energy, in the "calc" mode with "so" option for "hr", "hc" and "fc" potentials in absense of polarization potential (npl). Lower panel: same as upper panel but in the presence of a polarization potential (wpl).
See text (Section 4) for the meaning of the various labels.

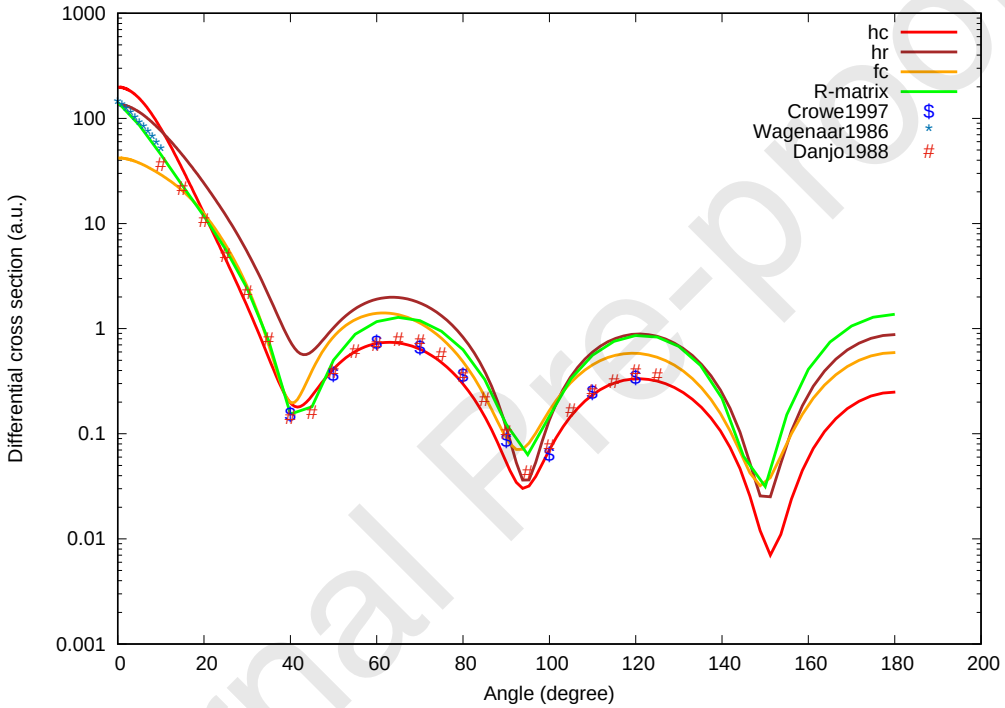


Figure 11: Comparison between DCS's for Krypton at 100 eV of impinging electron energy, in the "calc" mode with "so" option for "hr", "hc" and "fc" potentials. The experimental points are derived from [33] (symbol *), [34] (symbol #) and [35] (symbol $). The green curve represent the results for the DCS calculated using the (non-relativistic) R-matrix method by Fon *et al* [36]. See text (Section 4) for the meaning of the various labels.

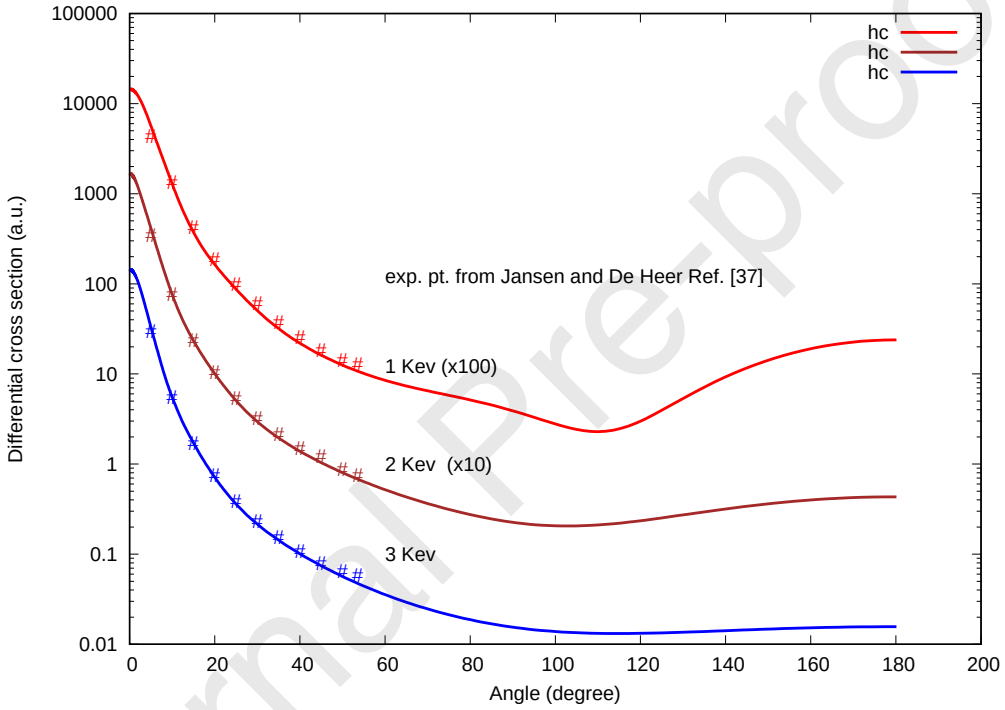


Figure 12: Krypton DCS spectra at 1, 2 and 3 Kev compared with the experimantal data by Jansen and De Heer [37]. For clarity, data at 1 Kev are multiplied by 100 and those at 2 Kev by 10 to fit on the same frame.

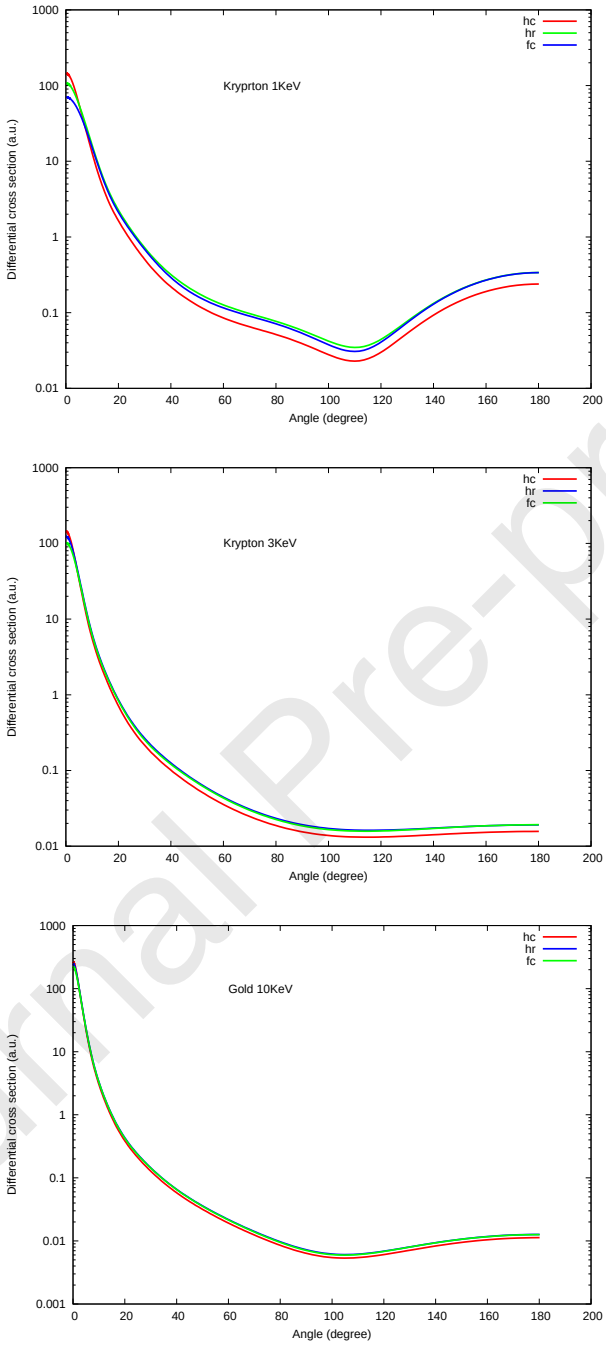


Figure 13: Upper panel: Calculated Krypton DCS spectra in the “calc” mode with “so” option for “fc”, “hr” and “hc” potentials at 1 Kev of incident energy. Middle panel: same as upper panel at 3 Kev. Lower panel: Calculated Gold DCS spectra in the “calc” mode with “so” option for “fc”, “hr” and “hc” potentials at 10 Kev of incident energy.

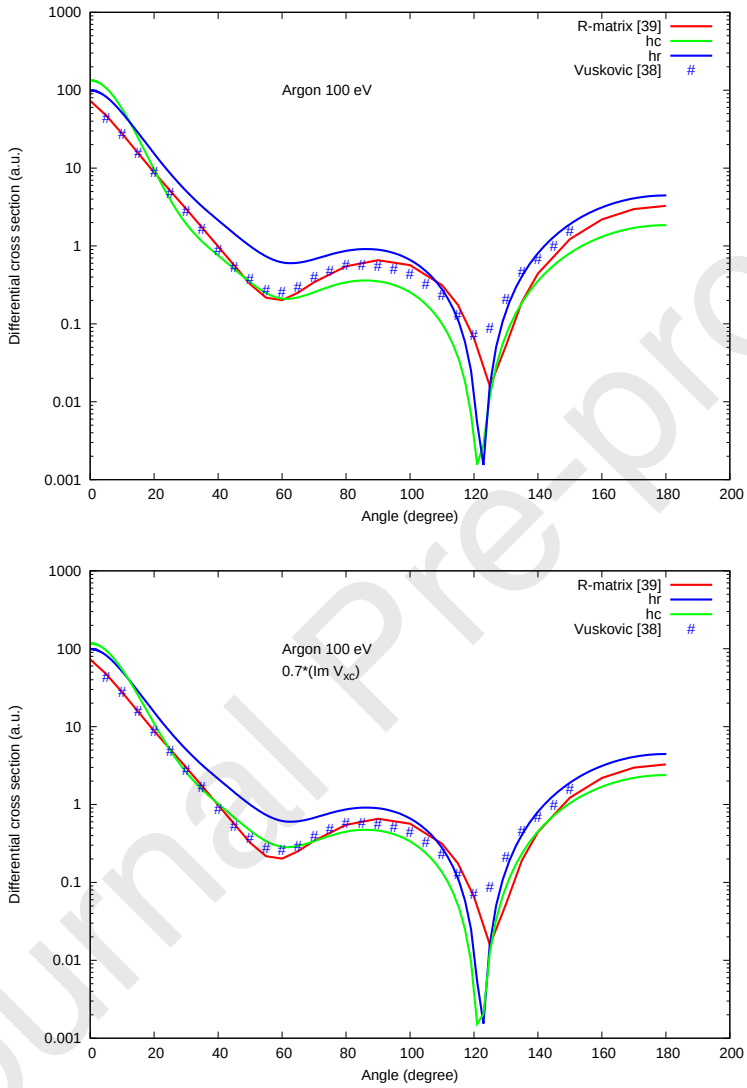


Figure 14: Upper panel: comparison between DCS's for Argon at 100 eV of impinging electron energy, in the "calc" mode with "so" option for "hr", "hc" potentials. The experimental points are derived from [38] (symbol #). The red curve represent the results for the DCS calculated using the (non-relativistic) R-matrix method by Fon *et al* [39]. Lower panel: same as upper panel but with the imaginary part of the HL potential reduced uniformly by a factor 0.7.

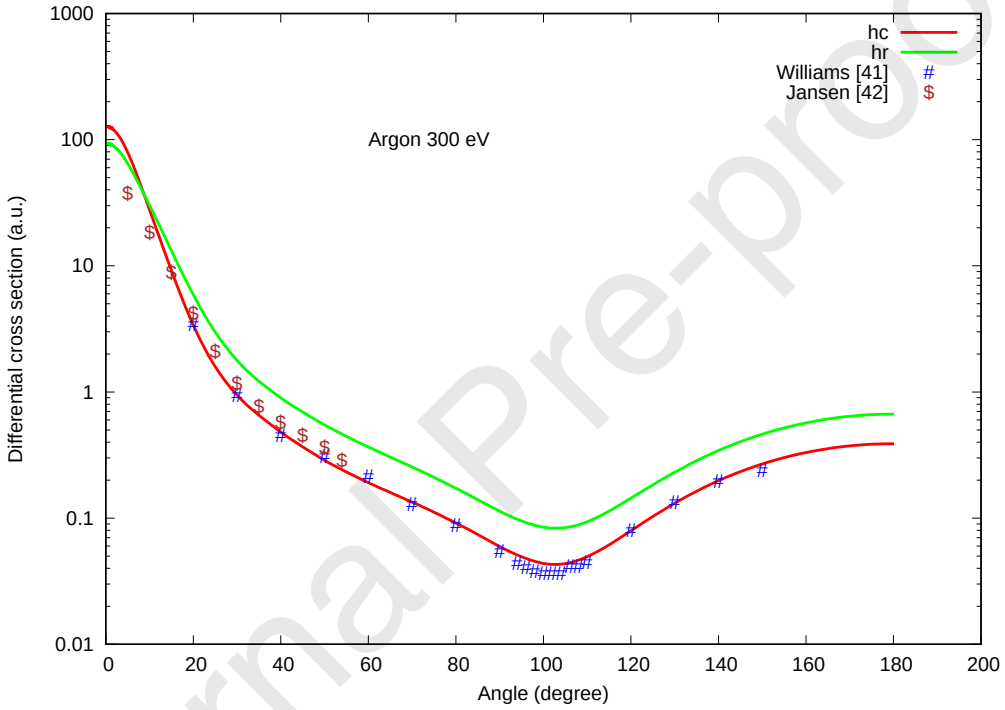


Figure 15: DCS for Argon at 300 eV of impinging electron energy, in the "calc" mode with "so" option for "hr", "hc" potentials. The experimental points are derived from [40] (symbol #) and [41] (symbol $).

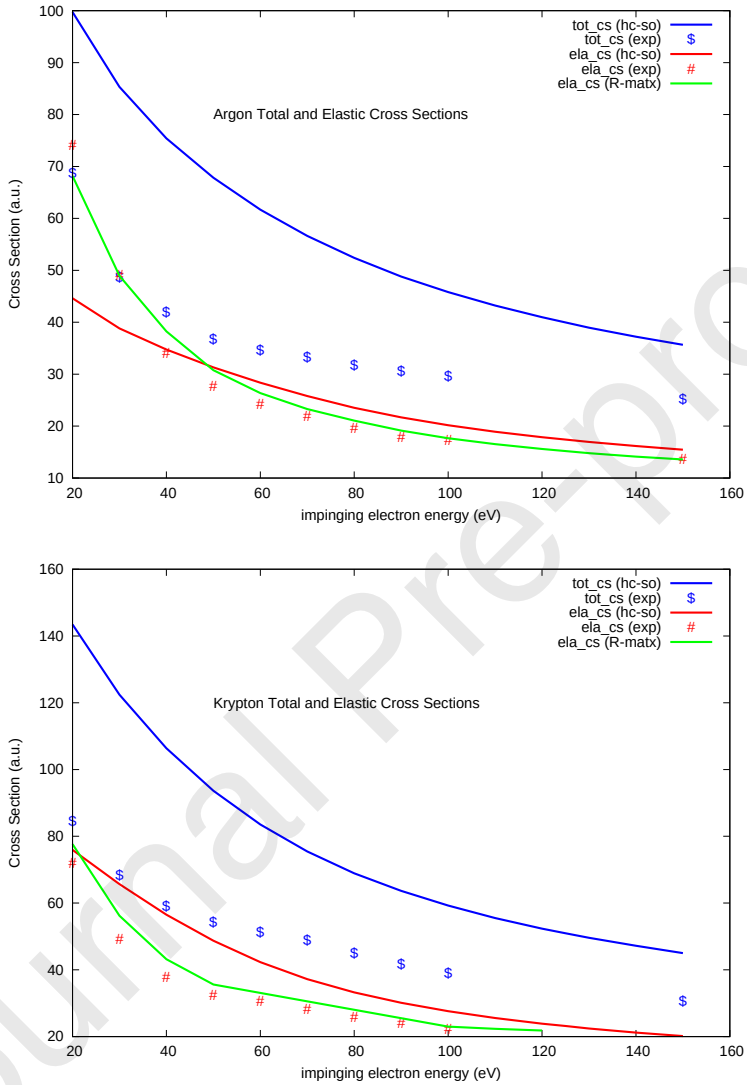


Figure 16: Upper panel: Comparison of integrated total and elastic CS for Argon, in the "calc" mode with "so" option using the "hc" potentials with the non relativistic R-matrix calculations of Ref. [39]. The experimental data for total CS were taken from Ref. [45], whereas those for the elastic CS were taken from Table 5 (column B) of Ref. [39]. Lower panel: Same as upper panel, but for Krypton, where the R-matrix calculation and the experimental data for the elastic CS were taken from Table 5 (column B) of Ref. [36], and those for the total CS again from Ref. [45].

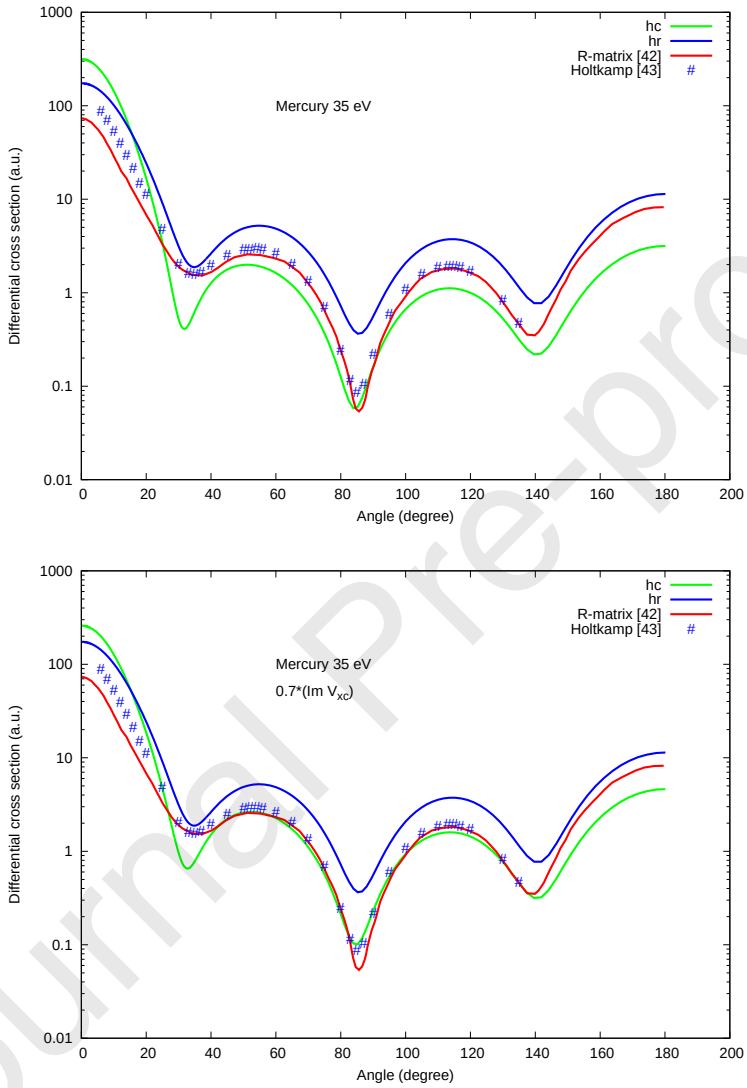


Figure 17: Upper panel: Comparison of the DCS's for Mercury at 35 eV of incident energy, in the "calc" mode with "so" option using the "hc" and the "hr" potentials with the relativistic R-matrix calculations [42]. The experimental data are taken from Ref. [43]. Lower panel: Same as upper panel, but with the imaginary part of the "hc" potential reduced uniformly by a factor 0.7. See text (Section 4) for the meaning of the various labels.

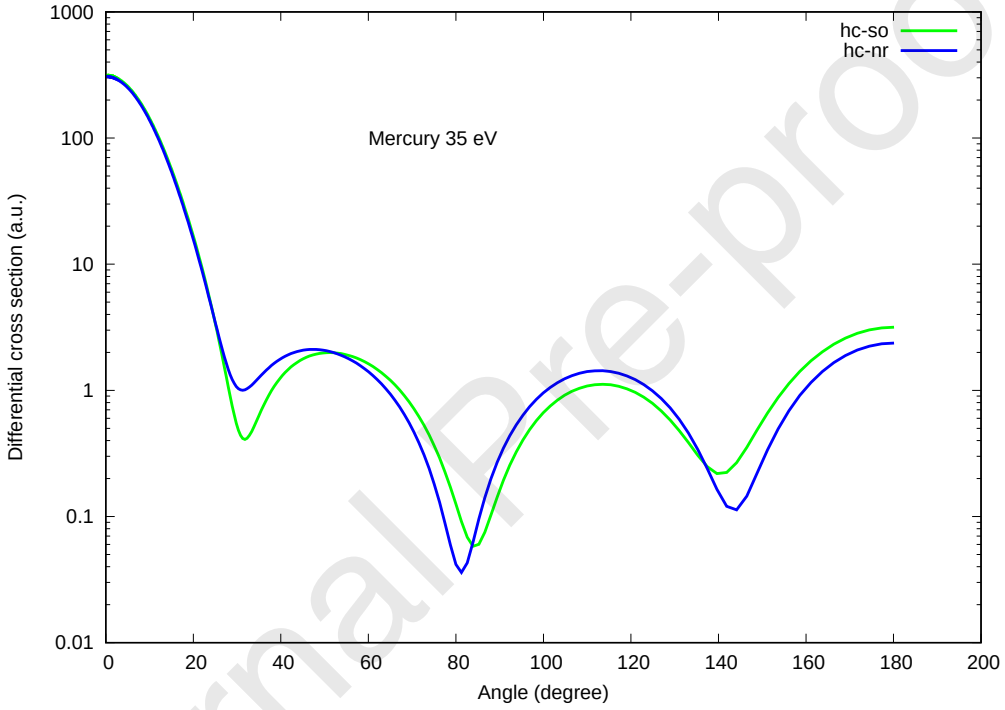


Figure 18: Comparison of the DCS's for Mercury at 35 eV of incident energy, in the "calc" mode between the relativistic "hc" potential with "so" option and the same potential with non relativistic"nr" option. See text (Section 4) for the meaning of the various labels.

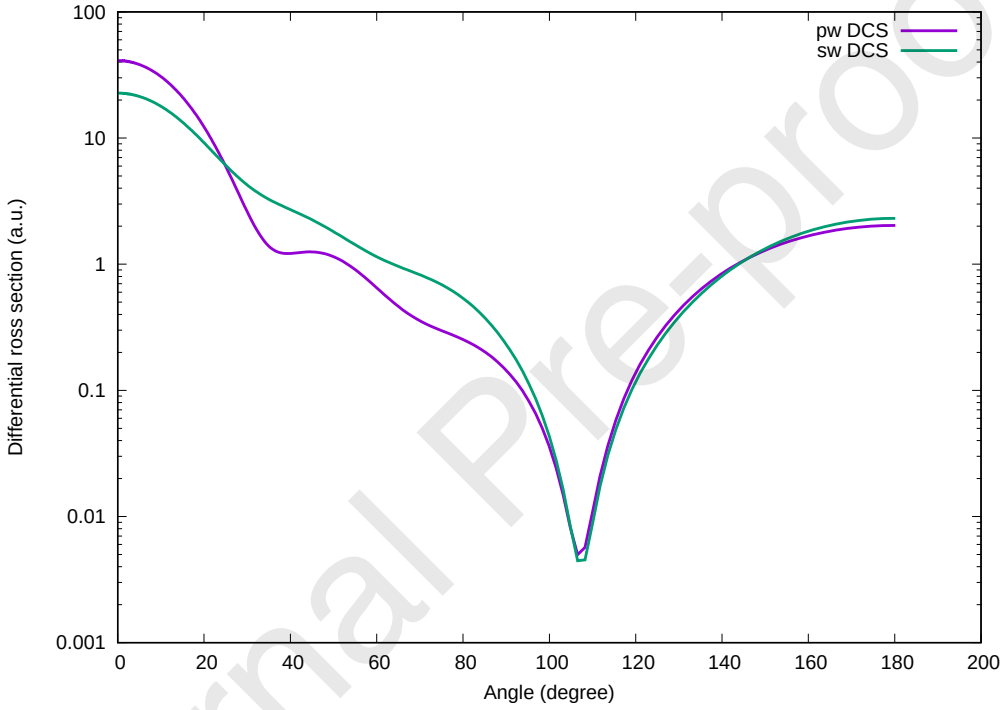


Figure 19: Comparison between DCS's calculated using plane wave (pw) and spherical wave (sw) propagators for Aluminum at 100 eV of impinging electron energy, in the "solid" mode with "sr" and "hc" options. See text (Section 4) for the meaning of the various labels.

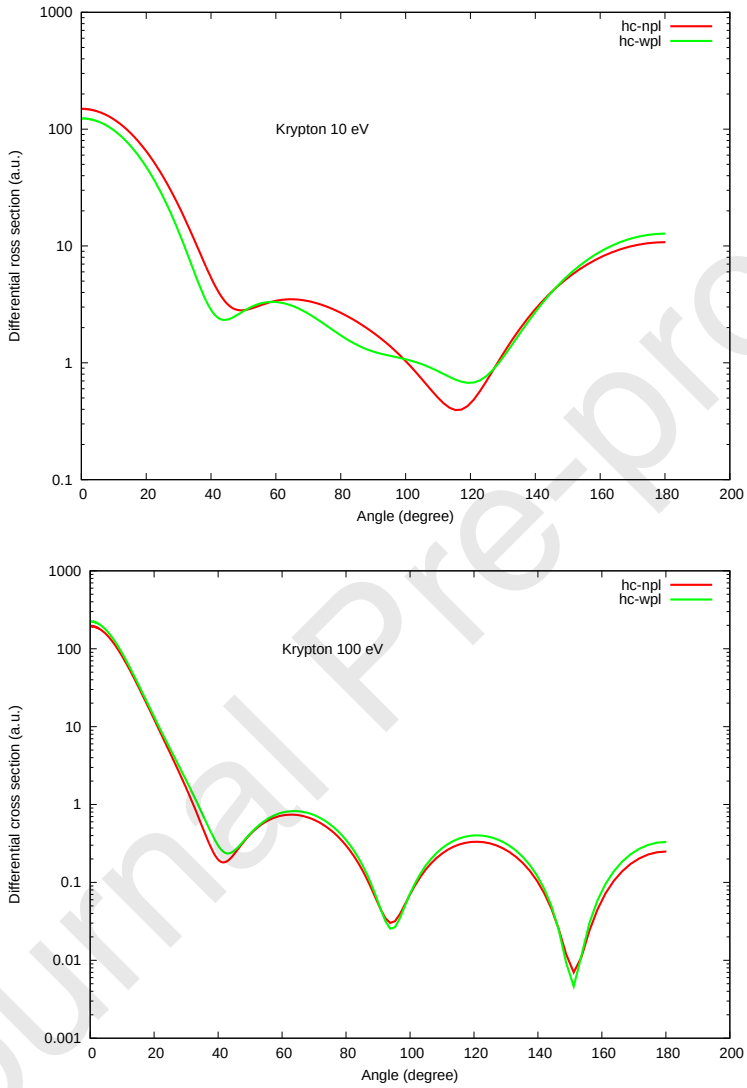


Figure 20: Comparison between DCS's for Krypton at 10 eV of impinging electron energy (upper panel) in the "calc" mode with "hc" and "so" options, in presence (labeled "hc-wpl") and in absence of the polarization potential (labeled "hc-npl"). Lower panel: Same comparison as in upper panel, but at 100 eV of impinging electron energy.
See text (Section 4) for the meaning of the various labels.

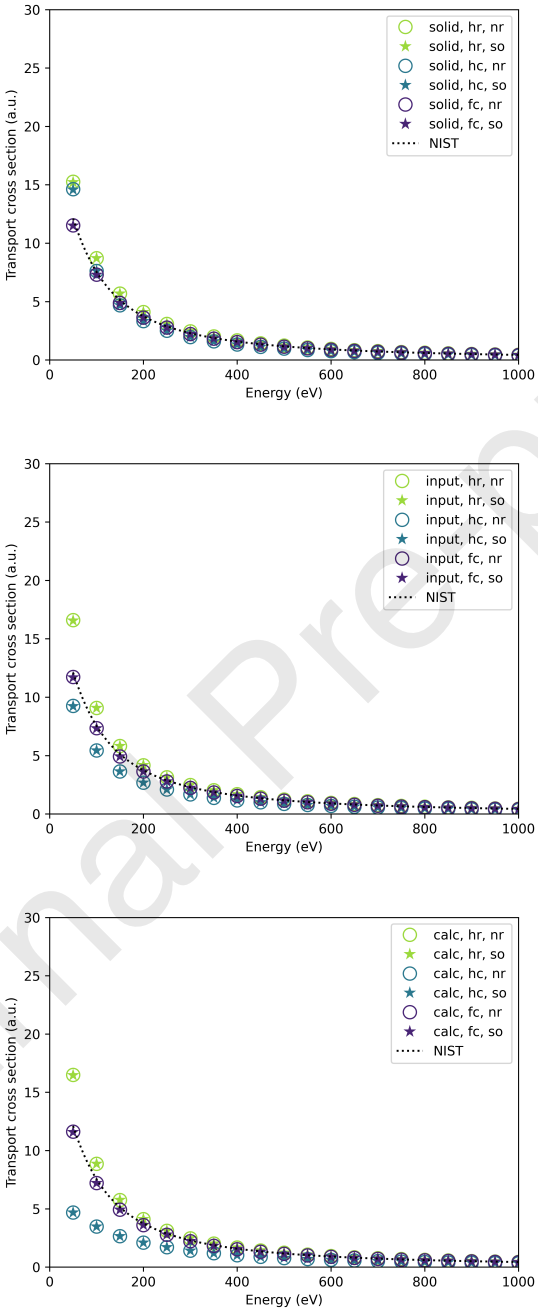


Figure 21: Calculated transport cross section for aluminum. See text (Section 4) for the meaning of the various labels.

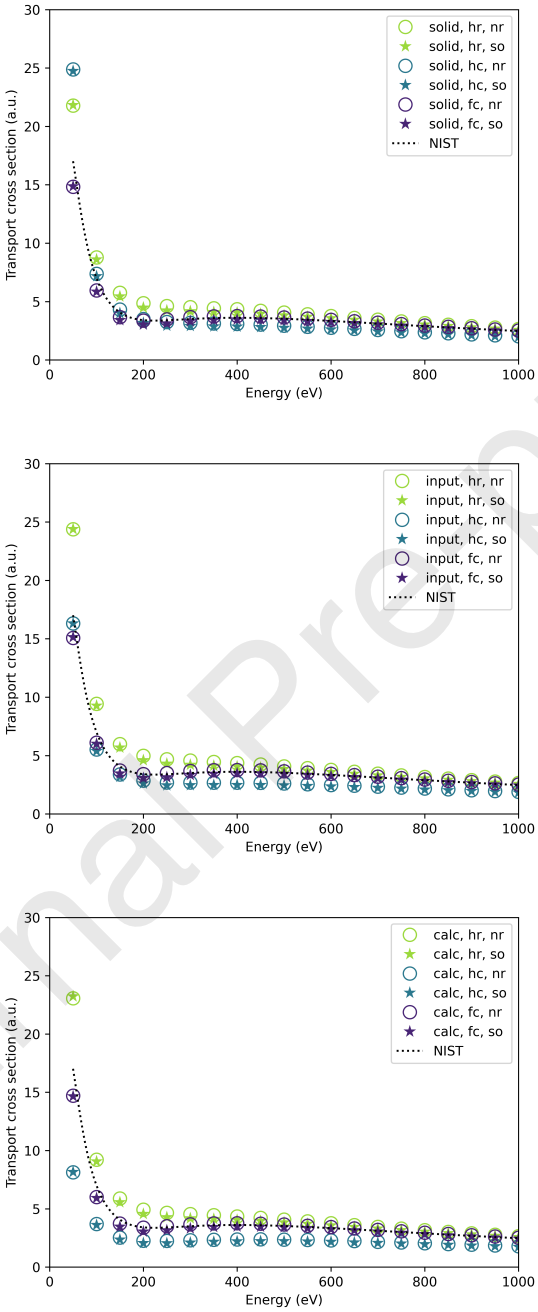


Figure 22: Calculated transport cross section for gold. See text (Section 4) for the meaning of the various labels.

**Declaration of interests**

☒ The authors declare that they have no known competing financial interests or personal relationships that could have appeared to influence the work reported in this paper.

☐ The authors declare the following financial interests/personal relationships which may be considered as potential competing interests: